Astronomy & Astrophysics manuscript no. lducci_ngc1512
May 15, 2014
©ESO 2014

arXiv:1405.3495v1 [astro-ph.HE] 14 May 2014

XMM-Newton observation of the interacting galaxies NGC 1512 and NGC 1510 ⋆,⋆⋆

L. Ducci[1,2], P. J. Kavanagh[1], M. Sasaki[1], and B. S. Koribalski[3]

[1] Institut für Astronomie und Astrophysik, Eberhard Karls Universität, Sand 1, 72076 Tübingen, Germany
e-mail: ducci@astro.uni-tuebingen.de
[2] ISDC Data Center for Astrophysics, Université de Genève, 16 chemin d'Écogia, 1290 Versoix, Switzerland
[3] Australia Telescope National Facility, CSIRO Astronomy and Space Science, PO Box 76, Epping, NSW 1710, Australia

ABSTRACT

Context. The galaxy NGC 1512 is interacting with the smaller galaxy NGC 1510 and shows a peculiar morphology, characterised by two extended arms immersed in an HI disc whose size is about four times larger than the optical diameter of NGC 1512.
Aims. For the first time we performed a deep X-ray observation of the galaxies NGC 1512 and NGC 1510 with *XMM-Newton* to gain information on the population of X-ray sources and diffuse emission in a system of interacting galaxies.
Methods. We identified and classified the sources detected in the *XMM-Newton* field of view by means of spectral analysis, hardness-ratios calculated with a Bayesian method, X-ray variability, and cross-correlations with catalogues in optical, infrared, and radio wavelengths. We also made use of archival *Swift* (X-ray) and Australia Telescope Compact Array (radio) data to better constrain the nature of the sources detected with *XMM-Newton*.
Results. We detected 106 sources in the energy range of 0.2−12 keV, out of which 15 are located within the D_{25} regions of NGC 1512 and NGC 1510 and at least six sources coincide with the extended arms. We identified and classified six background objects and six foreground stars. We discussed the nature of a source within the D_{25} ellipse of NGC 1512, whose properties indicate a quasi-stellar object or an intermediate ultra-luminous X-ray source. Taking into account the contribution of low-mass X-ray binaries and active galactic nuclei, the number of high-mass X-ray binaries detected within the D_{25} region of NGC 1512 is consistent with the star formation rate obtained in previous works based on radio, infrared optical, and UV wavelengths. We detected diffuse X-ray emission from the interior region of NGC 1512 with a plasma temperature of $kT = 0.68\ (0.31 - 0.87)$ keV and a 0.3–10 keV X-ray luminosity of 1.3×10^{38} erg s^{-1}, after correcting for unresolved discrete sources.

Key words. galaxies: individual; NGC 1512, NGC 1510 − X-rays: galaxies

1. Introduction

NGC 1512 and NGC 1510 are two interacting galaxies at a distance of ∼9.5 Mpc (Koribalski et al. 2004). NGC 1512 is a barred spiral galaxy (SB(r)a; de Vaucouleurs et al. 1991) with two star-forming rings and two extended arms immersed in an HI disc about four times larger than the optical diameter, probably caused by an ongoing tidal interaction with the neighbouring galaxy NGC 1510 (Kinman 1978). NGC 1510 is a blue compact dwarf galaxy separated by only ∼14 kpc from NGC 1512. Its blue colour and emission line spectrum are probably caused by the star formation activity produced by the interaction with NGC 1512 (Hawarden et al. 1979). Based on the analysis of the distribution and kinematics of the HI gas and the star formation activity in NGC 1512/1510, Koribalski & López-Sánchez (2009) concluded that the star formation activity in the outskirts of the disc as well as the distortion in the HI arms are the consequence of the interaction between the two galaxies that started about 400 Myr ago (Koribalski & López-Sánchez 2009). These authors used methods based on measurements of lines and continuum emission at different wavelengths (from radio to UV) to estimate the star formation rate (SFR) of both NGC 1512 and NGC 1510. They derived an average SFR of 0.22 $M_\odot$ yr^{-1} for NGC 1512 and $SFR = 0.07\ M_\odot$ yr^{-1} for NGC 1510.

To our knowledge, there has been no detection of sources at the position of NGC 1512/1510 with X-ray telescopes to date. From ROSAT/PSPC observations, O'Sullivan et al. (2001) derived a luminosity upper limit for NGC 1510 of $L_x \leq 5.8 \times 10^{39}$ erg s^{-1} (0.1 − 2.4 keV). Therefore, the work described in this paper represents the first report of significant X-ray emission in NGC1512/1510. The *XMM-Newton* observation on which this paper is based (see Sect. 2) allows the detection of the brightest populations of X-ray sources ($L_x \gtrsim 10^{37}$ erg s^{-1}) typically observed in normal galaxies. The main class of galactic X-ray sources is that of X-ray binaries (XRBs), whose X-ray luminosity, ranging from $\sim 10^{32}$ to $\sim 10^{39}$ erg s^{-1}, is produced by the accretion of matter from the donor star to a compact object (a neutron star or a black hole). XRBs are conventionally divided into two classes according to the nature of the donor star: low-mass X-ray binaries (LMXBs) and high-mass X-ray binaries (HMXBs). LMXBs host late-type stars and have a lifetime of $\sim 10^7 - 10^9$ yr because of the nuclear timescale of the donor star. Their number is roughly proportional to the total stellar mass of the galaxy (e.g. Gilfanov 2004). HMXBs host early-

⋆ Based on observations obtained with *XMM-Newton*, an ESA science mission with instruments and contributions directly funded by ESA Member States and NASA. The radio observations were obtained with the Australia Telescope Compact Array, which is part of the Australia Telescope National Facility funded by the Commonwealth of Australia for operation as a National Facility managed by CSIRO.
⋆⋆ Tables B.1 and B.2 are only available in electronic form at the CDS via anonymous ftp to cdsarc.u-strasbg.fr (130.79.128.5) or via http://cdsweb.u-strasbg.fr/cgi-bin/qcat?J/A+A/

type stars and have a lifetime of $\sim 10^6 - 10^7$ yr. Therefore, their number is proportional to the recent SFR of a galaxy (e.g. Grimm et al. 2003).

Large-scale diffuse X-ray emission in galaxies can be used to trace outflows and feedback processes on galactic scales. Such emission has been detected with the current generation of X-ray observatories in many nearby galaxies, including M31 (Shirey et al. 2001), M101 (Kuntz et al. 2003), NGC 300 (Carpano et al. 2005), NGC 6946 (Schlegel et al. 2003), NGC 1672 (Jenkins et al. 2011), and NGC 253 (Bauer et al. 2008). As such, the NGC 1512/1510 system may also exhibit diffuse X-ray emission that can be used to investigate these physical processes.

In this paper we report the results obtained from a study of the X-ray sources in the *XMM-Newton* field of view of NGC 1512/1510. The paper is organised as follows: in Sect. 2 we present the *XMM-Newton*, *Swift*, and Australia Telescope Compact Array (ATCA) observations on which our work is based and the analysis of the data. In Sect. 3 we describe the methods adopted to classify the sources based on their X-ray properties and the analysis of X-ray diffuse emission from NGC 1512. In Sect. 4 we cross-correlate the list of sources detected with *XMM-Newton* with radio, infrared, and optical catalogues and discuss the identifications and classifications obtained for some of these sources. In Sect. 5 the results for point sources and X-ray diffuse emission are discussed.

2. Observations and data reduction

2.1. XMM-Newton: *source detection*

The galaxy pair NGC 1512/1510 has been observed with *XMM-Newton* (ID: 0693160101) between 2012 June 16 (20:31 UTC) and 2012 June 17 (16:24 UTC) in a single, 63 ks exposure observation. The data analysis was performed through the *XMM-Newton* Science Analysis System (SAS) software (version 12.0.1). The observation was largely contaminated by high background due to proton flares. After rejecting time intervals affected by high background, the net good exposure time was reduced to 26.0 ks for PN, 39.8 ks for Metal Oxide Semi-conductor 1 (MOS1), and 34.8 ks for MOS2.

For each instrument, data were divided into five energy bands:

- B_1: 0.2–0.5 keV;
- B_2: 0.5–1 keV;
- B_3: 1–2 keV;
- B_4: 2–4.5 keV;
- B_5: 4.5–12 keV.

For the PN, data were filtered to include only single events (PATTERN=0) in the energy band B_1, and single and double events (PATTERN≤4) for the other energy bands. We excluded the energy range 7.2 – 9.2 keV to reduce the background produced by strong fluorescence lines in the outer detector area (Freyberg et al. 2004). For the MOS, single to quadruple events (PATTERN≤12) were selected.

We ran the source detection using the SAS task `edetect_chain` on the images corresponding to the five energy bands and three instruments (total of 15 images) simultaneously. The source detection procedure can be divided into three steps. The first step creates temporary source lists and background maps for these source lists. Local background maps are then used to detect the sources. We adopted a minimum-detection likelihood of 7 to obtain the list of sources (the detection likelihood L is defined by $L = -\ln p$, where p is the probability that a Poissonian fluctuation of the background is detected as a spurious source). To create the background maps the sources are removed from the images and a two-dimensional spline with 16 nodes is fitted to the exposure-corrected image. In the second step the background maps are used to improve the detection sensitivity and hence to create a new source list. Here we adopted a minimum-detection likelihood of 4. In the last step, the list of source positions obtained in the previous step is used to perform a maximum-likelihood point-spread function (PSF) fit to the source count distribution simultaneously in all energy bands and each EPIC instrument (a description of this algorithm is given by Cruddace et al. 1988). For this step we adopted a minimum likelihood of $L = 6$. This step provides the final source list. The source detection procedure of the task `edetect_chain` provides, for each detected source, many parameters such as the position, the positional error, count rate, likelihood of detection, and hardness ratios (see Table B.1). We removed false detections (artefacts on the detectors or diffuse emission structures) by visual inspection. We detected 106 sources in the NGC 1512/1510 field of view.

Figure 1 shows the combined PN, MOS1, and MOS2 three-colour *XMM-Newton* image. The numbers of the detected sources in Table B.1 are overplotted on the image. The thick green ellipses are the D_{25} ellipses for NGC 1512 and NGC 1510 (de Vaucouleurs et al. 1991) defined by the 25 mag arcsec^{-2} B-band isophote.

2.2. XMM-Newton: *diffuse emission*

To search for extended X-ray emission in the NGC 1512/1510 system we used the *XMM-Newton* Extended Source Analysis Software (XMM-ESAS), packaged in SAS 12.0.1. This program is based on the software used for the background modelling described in Snowden et al. (2004). Essentially, XMM-ESAS consists of a set of tasks to produce images and spectra from observational data and to create quiescent particle background (QPB) images and spectra that can be subtracted from the observational science products (see Kuntz & Snowden 2008; Snowden et al. 2008). To ensure compatibility of our analysis with the XMM-ESAS framework, we reprocessed the observational data according to the ESAS cookbook[1]. Standard filtering and calibration were applied to the observational data using the XMM-ESAS tools `epchain`, `emchain`, `pn-filter`, and `mos-filter`. The CCDs of each of the EPIC instruments were then examined to ensure that none were operating in an anomalous state (where the background at $E < 1$ keV is strongly enhanced, see Kuntz & Snowden 2008). We determined that CCD 4 of the EPIC-MOS1 was in an anomalous state and excluded it from further analysis. The tasks `pn-filter` and `mos-filter` clean the data of obvious soft-proton (SP) flares by calling the task `espfilt`. After filtering with `espfilt`, 16 ks of EPIC-PN data, and 27 ks and 25 ks of EPIC-MOS1 and EPIC-MOS2 data, respectively, were available for further analysis. Since this observation was highly affected by SP flares, the likelihood of substantial residual SP contamination is high. We estimated the level of this using the diagnostic tool of De Luca & Molendi (2004)[2]. Unfortunately, the filtered event lists of each of the EPIC in-

[1] Available at `http://heasarc.gsfc.nasa.gov/docs/xmm/xmmhp_xmmesas.html`

[2] Available at `http://xmm2.esac.esa.int/external/xmm_sw_cal/background/epic_scripts.shtml#flare`

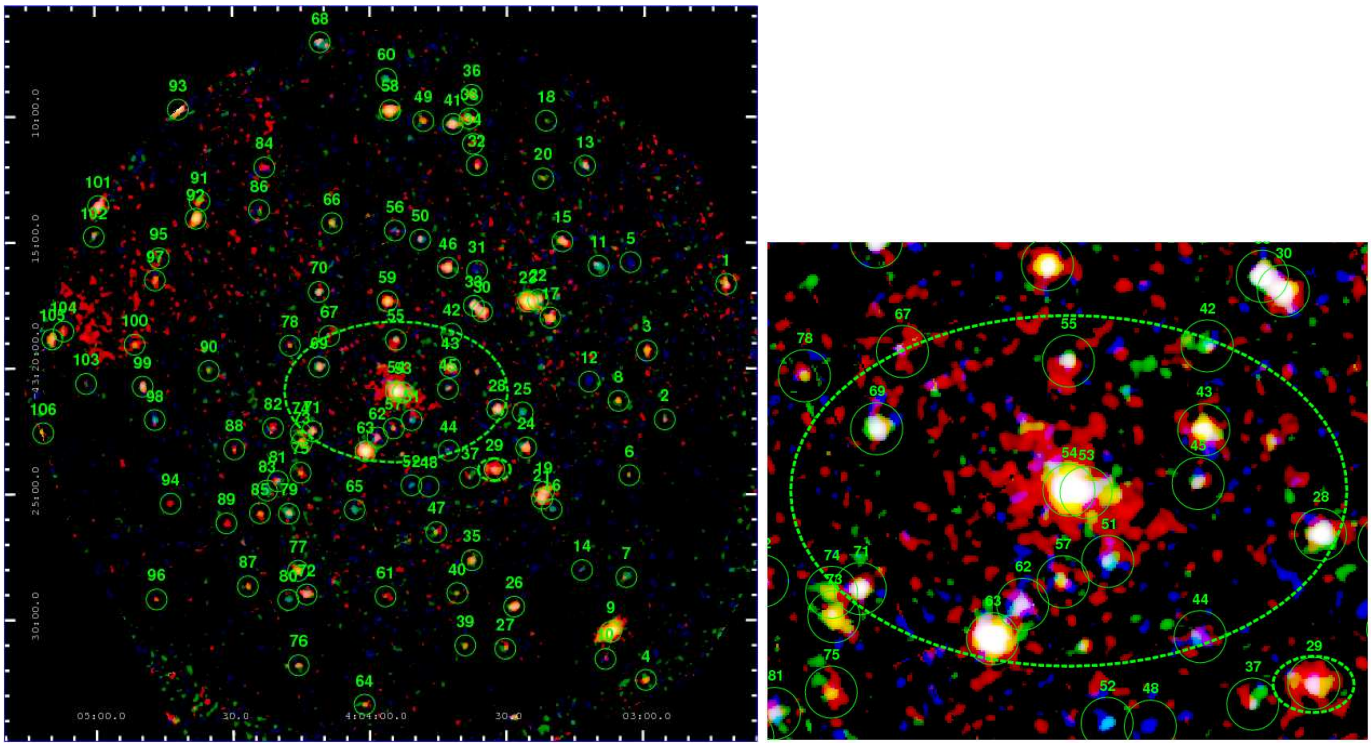

Fig. 1. Combined PN, MOS1, and MOS2 three-colour mosaic image of the NGC 1512/1510 field of view, where red, green, and blue colors represent the 0.2 – 1 keV, 1 – 2 keV, 2 – 4.5 keV energy bands. The green dashed ellipses are the D_{25} ellipses for NGC 1512 and NGC 1510. The right panel shows a close-up view of the central region.

struments were flagged as being 'extremely' contaminated by SPs. Therefore, we proceeded very tentatively and cautiously with our search for extended emission in the NGC 1512/1510 system.

We excluded point sources determined in Sect. 2.1 from the observational data using the SAS task `region` and the XMM-ESAS task `make_mask`. The contour method of the `region` task was used to define the exclusion regions. The task calculates the point spread function (PSF) at the source position and normalises for the source brightness. Source counts were then removed down to a PSF threshold of 0.25 times the local background, that is, the point source is excluded down to a level where the surface brightness of the point source is one quarter of the surrounding background. This method has the advantage that the point source exclusion regions follow the brightness of the source, so that brighter sources have larger exclusion regions and shapes corresponding approximately to the source PSF. Hence, the number of diffuse counts is maximised by tailoring the point source exclusion regions to the individual sources. By excluding counts in this manner, contamination from the point sources is reduced to a negligible level.

The `pn-spectra` and `mos-spectra` were used to produce images with the point sources masked in the 0.3-2 keV and 2-7 keV energy bands. The `pn-back` and `mos-back` tasks were then used to produce corresponding QPB images. Using XMM-ESAS, it is also possible to model and retrospectively subtract residual SP contamination from the images. To this end we extracted full-field spectra and QPB backgrounds for the EPIC instruments and fitted the spectra in the 3–7 keV energy range where the SP contamination is expected to dominate (see Section 3.4.1 for a description of the SP fitting process). The determined spectral parameters were then used to generate model SP contamination images with the XMM-ESAS task `proton`. The `comb` task was used to merge the observational QPB images and SP images from all three EPIC instruments into combined EPIC images. Finally, the `adapt-900` task was run to subtract the QPB and SP background, and adaptively smooth the resulting images. We note here that solar wind charge-exchange emission (SWCX), which is correlated to enhancements in the solar wind (Snowden et al. 2004), may also affect our observation. This is discussed in more detail in Section 3.4.3, but the effect is expected to be uniform across the FOV and, thus, it is only necessary to adjust the background flux levels. While no extended emission was observed in most of the NGC 1512/1510 field, there was evidence for faint soft emission in the innermost region of NGC 1512, illustrated in Figure 2 (left). Morphologically, the diffuse X-ray emission appears to be associated with the region of the UV ring of NGC 1512 (Koribalski & López-Sánchez 2009), shown in Figure 2 (middle), which also corresponds to the region of higher stellar density, as evident from the K_s-band image taken from the 2MASS Large Galaxy Atlas[3] (Jarrett et al. 2003), Figure 2 (right).

2.3. Swift/XRT

NGC 1512 and NGC 1510 have been observed with the X-ray Telescope (XRT; Burrows et al. 2005), one of the three instruments on board the *Swift* satellite (Gehrels et al. 2004), from July 2011 to January 2013, for a total exposure time of ∼ 33.6 ks.

We used these data to study the long-term X-ray variability of sources detected with both *Swift*/XRT and *XMM-Newton*/EPIC (see Sect. 3.3). We collected the XRT observations in two groups: *obs1:* from 2011/07/26 00:13:25

[3] Available at `http://irsa.ipac.caltech.edu/applications/2MASS/LGA/`

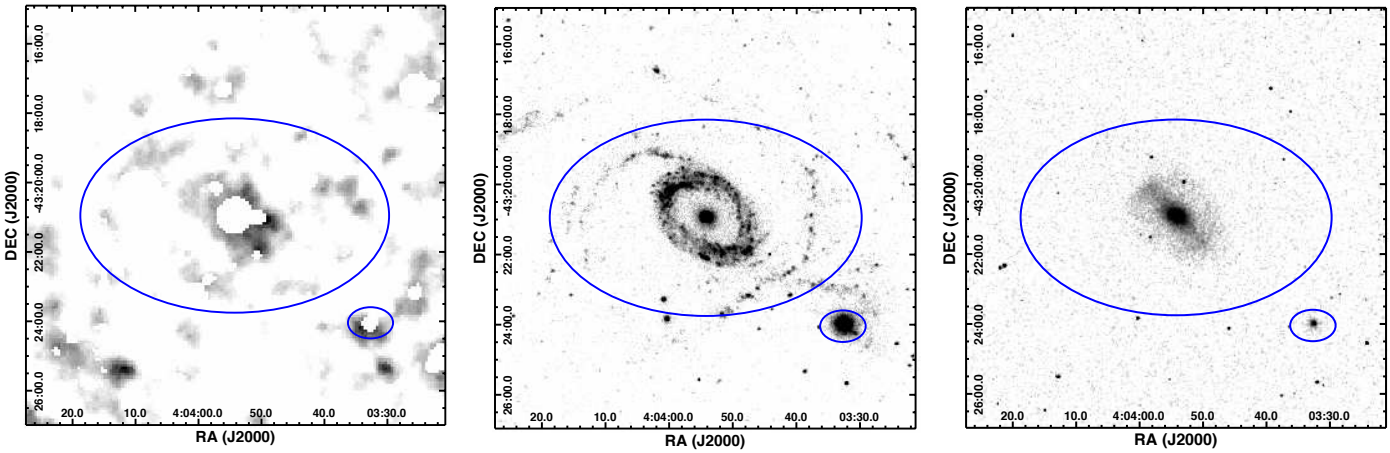

Fig. 2. *Left*: combined EPIC 0.3-2 keV image of the inner region of the NGC 1512/1510 observation. The image has been corrected for QPB and SP contamination, binned into 2x2 pixel bins before being adaptively smoothed using the XMM-ESAS task `adapt-900`. *Middle*: *Swift*/UVOT image (uvm2 filter) of NGC 1512/1510. *Right*: 2MASS K_s-band image of NGC 1512/1510 taken from the 2MASS Large Galaxy Atlas (Jarrett et al. 2003). The blue ellipses represent the D_{25} ellipses for the galaxy pair.

Table 1. *Swift*/XRT observations of NGC 1512/1510.

ObsID	Start date	$T_{\rm exp}$ (ks)
00045603001	2011-07-26 00:13:25	3077.8
00045603002	2011-08-01 07:10:01	2880.3
00045603003	2011-08-02 07:21:12	1965.2
00045603004	2011-08-04 00:59:00	767.2
00045603005	2011-08-05 05:49:01	2447.1
00045603008	2012-09-25 01:09:59	9497.0
00045603009	2012-09-26 01:09:59	3778.5
00045603010	2012-09-27 04:50:59	4588.0

to 2011/08/05 05:49:01; *obs2:* from 2012/09/25 01:09:59 to 2012/09/27 04:50:59 (see Table 1). We processed the XRT data obtained in photon-counting mode (PC) with the standard procedures (xrtpipeline v0.12.6; Burrows et al. 2005). For each group of observations, source detection was performed using `XIMAGE` (v4.5.1). For each source, we obtained the count rate and significance using the source statistics (`sosta`) tool within `XIMAGE`. The sources detected by *Swift*/XRT with a signal-to-noise ratio $S/N > 3$, not located at the edge of the field of view (where the high background noise can be misinterpreted as real sources by the source detection procedure), and with a unique *XMM-Newton* counterpart are sources No. 54 (the nuclear region of NGC 1512) and No. 63. Owing to the low angular resolution of *Swift*/XRT, the pairs of *XMM-Newton* sources 30/33, 38/41, and 91/92 have been detected by XRT as three sources. Therefore, for the long-term variability study we only considered sources No. 54 and 63 (see Sect. 3.3).

2.4. ATCA

The system NGC 1512/1510 has been observed in radio (20-cm) with ATCA. The observation consists of four pointings with multiple configurations (see Koribalski & López-Sánchez 2009 for the observing and data reduction details).

We used the 20-cm radio continuum maps with 8 and 15 arcsec resolution to find possible radio counterparts of the X-ray sources we detected with *XMM-Newton*. We found nine radio counterparts of sources 13, 23, 29 (nuclear region of NGC 1510), 54 (nuclear region of NGC 1512), 67, 71, 83, 94, and 98. We used these associations to classify five background objects (see Sect. 4.2).

3. Analysis

3.1. Astrometrical corrections

We determined the systematic errors in the X-ray positions of the *XMM-Newton* observation by calculating the offsets in the X-ray positions of the *XMM-Newton* sources identified and/or classified as foreground stars and background objects (see Sect. 4) with respect to their optical and infrared counterparts (USNO-B1 and 2MASS catalogues of Monet et al. 2003 and Cutri et al. 2003). In particular, we used the sources of Tables 5 and 6, which were clearly identified as foreground or background objects except for source No. 61, which appears to be extended on the DSS maps. The offset between the X-ray positions and the optical positions corrected for proper motion is $\Delta RA = -0.41 \pm 0.54$ arcsec, $\Delta Dec = -1.44 \pm 0.54$ arcsec. Since the offset for *RA* is not statistically significant, we used only ΔDec to correct the positions of all the detected sources. The rms offsets in declination before and after correction are 2.4 and 2.1.

3.2. Spectral analysis and hardness ratios of point sources

We extracted the X-ray spectra of the sources from circular or elliptical regions, which were adjusted by eye for each source on each detector, depending on the presence of nearby sources. Background spectra were extracted from source-free zones and then normalised to the extraction area of the corresponding source. The spectra, instrument responses, and ancillary files were generated using the SAS software. We performed the spectral analyses using `XSPEC` (ver. 12.7.0, Arnaud 1996a).

For brighter sources (counts $\gtrsim 300$ in the energy range $0.2 - 12$ keV) we used the χ^2 statistics. The spectral energy channels were grouped to have at least 20 counts per bin for good statistical quality of the spectra.

For sources with a fewer counts we used the Cash statistic (or C-stat; Cash 1979), which allows background subtraction

in XSPEC by means of the W-statistic[4]. W-statistic requires at least one count per spectral bin. We computed the quality of the fit with the XSPEC command goodness, which performs Monte Carlo simulations of 10^4 spectra from the best-fit model and provides the percentage of simulated spectra with a C-stat less than that obtained from the real data. If the model represents the data accurately, the goodness should be close to 50%.

We fitted the PN and MOS spectra simultaneously with different models. A good fit with one of these models can be used to classify the sources into one of the following classes:

- XRBs: power-law with $\Gamma = 1-3$; disc-blackbody with $kT_{\rm in} = 0.5 - 1$ keV (White et al. 1995; Makishima et al. 1986);
- supernova remnants: a thermal plasma model (e.g. apec of Smith et al. 2001 with $kT = 0.2 - 1.5$ keV);
- super-soft sources: blackbody with $kT_{\rm bb} = 50 - 100$ eV (Di Stefano & Kong 2003).

In total we fitted the spectra of eight sources. With the exception of source No. 9 (see Sects. 4.1 and A.1), the X-ray spectra can be fitted with an absorbed power-law or an absorbed disc-blackbody model, with photon indices and $kT_{\rm in}$ compatible with either XRBs or AGNs (see Sects. 4.2 and 4.3).

For each source, we calculated four hardness ratios, defined as

$$HR_i = \frac{B_{i+1} - B_i}{B_{i+1} + B_i} \text{ for } i = 1, ..., 4. \quad (1)$$

We calculated the hardness ratios of Eq. (1) with the Bayesian method described in Park et al. (2006) and implemented in the BEHR code[5] (ver. 08-28-2012). This method is based on the assumption that the detection of X-ray photons is a random process described by Poisson statistics instead of the classically assumed Gaussian statistic. The hardness ratios calculated using the Bayesian method are much more accurate than those calculated using the classical methods, especially for very faint sources, for which the Poisson distribution becomes more asymmetric. Moreover, if the source is not detected in one or more energy bands, the Bayesian method of Park et al. (2006) can produce reliable estimates where classical methods would fail. The required inputs for the Bayesian method of Park et al. (2006) are the source region counts, the background region counts (both corrected for vignetting and out-of-time events), the ratio of the source and background extraction areas, and the exposure time at the source position.

Hardness ratios can provide information about the X-ray properties of faint sources, for which the spectral fitting is not possible (see e.g. Prestwich et al. 2003). The hardness ratios calculated for each source are listed in Table B.1. Figure 3 shows the hardness ratios of the sources detected by *XMM-Newton* in NGC 1512/1510 (see Sect. 4.3). The grids of hardness ratios calculated for different spectral models, with $N_{\rm H}$ ranging from 10^{20} cm^{-2} to 10^{24} cm^{-2}, can help to better separate different classes of sources.

3.3. Variability analysis

For each XMM-*Newton* observation, we searched for pulsations of the brightest sources (counts $\gtrsim 100$) on time scales between ~ 0.15 s and the time duration of each observation. After extracting the event files, we applied both a Fourier transform and a Z_n^2

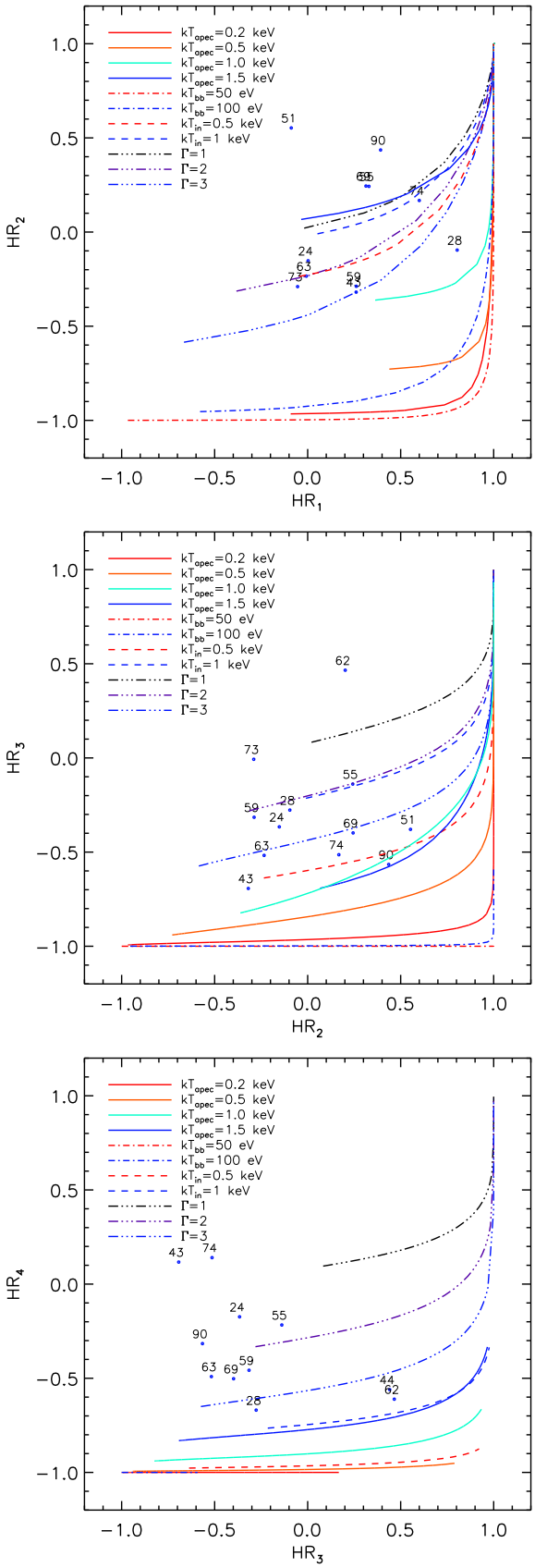

Fig. 3. Hardness-ratio diagrams of sources with error bars smaller than 0.3 detected in NGC 1512/1510. The lines are the hardness ratios calculated for different spectral models and column densities, as described in Sect. 3.2.

[4] see appendix 13 of XSPEC manual http://heasarc.nasa.gov/xanadu/xspec/manual/XSappendixStatistics.html

[5] See http://hea-www.harvard.edu/astrostat/behr/

Table 3. 0.5 – 10 keV fluxes, variability factor and significance of the variability of sources observed with *XMM-Newton* and *Swift*/XRT (flux in erg cm^{-2} s^{-1}).

No.	obs1 (Jul-Aug 2011) (*Swift*)	Jun. 2012 (*XMM-Newton*)	obs2 (Sept. 2012) (*Swift*)	V_f	S
54	$1.2^{+1.9}_{-0.6} \times 10^{-13}$	$6.7^{+2.0}_{-2.0} \times 10^{-14}$	$1.1^{+0.6}_{-0.5} \times 10^{-13}$	1.8	0.8
63	$7.5^{+3.0}_{-2.6} \times 10^{-14}$	$7.4^{+1.1}_{-1.0} \times 10^{-14}$	$1.2^{+0.4}_{-0.3} \times 10^{-13}$	1.6	1.4

Table 2. Count rate to energy conversion factors for thin and medium filters of the EPIC instruments in the energy ranges B1-B5, assuming an absorbed power-law with a photon index of 1.7 and the Galactic foreground absorption 1.9×10^{20} cm^{-2} in the direction of NGC 1512/1510.

Detector EPIC	Filter	B1	B2	B3	B4	B5
			(10^{-12}) erg cm^{-2} ct^{-1}			
PN	Medium	1.070	1.106	1.725	4.969	17.47
MOS	Medium	7.205	5.614	5.181	13.71	69.62

analysis (Buccheri et al. 1983) for one to three harmonics. No statistically significant variability from the analysed sources was detected.

We studied the long-term X-ray variability of sources detected with both *Swift*/XRT and *XMM-Newton*/EPIC. This was the case only for the two sources No. 54 and 63. We calculated the *XMM-Newton* fluxes with the energy conversion factors reported in Table 2. Table 3 shows the 0.5 – 10 keV *Swift* and *XMM-Newton* fluxes, variability factor $V_f = F_{max}/F_{min}$ (where F_{max} and F_{min} are the highest and lowest fluxes) and the significance of the variability $S = (F_{max} - F_{min})/\sqrt{\sigma^2_{max} + \sigma^2_{min}}$, where σ_{max} and σ_{min} are the errors of the highest and lowest flux (Primini et al. 1993). We derived the XRT fluxes from the count rates obtained with the tool `sosta` and the spectral parameters obtained in the *XMM-Newton* data analysis, assuming no changes in the spectral shape (see Table 7). Sources No. 54 and 63 do not show a significant ($S \geq 3$) variability.

3.4. Spectral analysis of diffuse emission

The spectral analysis of the region of soft diffuse emission in the centre of NGC 1512 is complicated because of the high residual SP contamination and the possible contribution of fainter, large-scale emission in NGC 1512 and/or SWCX emission. While these may not be so problematic for bright extended emission, the faint nature of the central diffuse emission required us to treat the background with utmost care to extract the purest possible spectral results. Since any additional faint contribution from NGC 1512 most likely varies across the FOV, a straightforward background extraction and subtraction from a nearby region may not be appropriate. In addition, backgrounds selected in this manner from different regions of the detector with different responses may also compromise our results. For these reasons, we decided to use XMM-ESAS techniques for the spectral analysis, that is, we subtracted the modelled QPB spectra and accounted for the remaining X-ray background by including a physically motivated model in the fits.

The XMM-ESAS tasks `pn-spectra` and `mos-spectra` were used to extract the spectra and response files from the emission region within the ring of NGC 1512 (see Fig. 2). `pn-back` and `mos-back` were used to produce corresponding QPB spectra to be subtracted from the observational spectra. The spectra, associated response files, and QPB spectra were linked using the `grppha` task in the FTOOLS package[6]. The spectra were grouped to at least 30 counts per bin to allow the use of the χ^2-statistic. All fits were performed using `XSPEC` (Arnaud 1996b) version 12.7.1 with ATOMDB[7] version 2.0.1, abundance tables set to those of Wilms et al. (2000), and photoelectric absorption cross-sections set to those of Balucinska-Church & McCammon (1992). We limited our analysis to > 0.4 keV to avoid the to strong low-energy tail due to electronic noise, as recommended in the ESAS cookbook. Following the subtraction of the QBP spectrum, we accounted for the remaining constituents of the X-ray background in `XSPEC`. These fall into two categories: the particle-induced background and the astrophysical background.

3.4.1. Particle-induced background

After subtracting the QPB, the remaining particle-induced background consists of instrumental fluorescence lines and the residual SP contamination. The instrumental fluorescence lines were modelled with Gaussian components (`gauss` in `XSPEC`) at 1.49 keV in the EPIC-PN spectrum, and 1.49 keV and 1.75 keV for the EPIC-MOS spectra. Additional instrumental lines are present at harder energies in the EPIC spectra, but because we limited our analysis to the 0.4-5 keV energy range, these were ignored. The residual SP contamination was modelled with a power-law (`powerlaw` in `XSPEC`) component not folded through the instrumental response. This is possible by using the diagonal response matrices supplied in the CALDB of XMM-ESAS. Given the small extraction area of the inner NGC 1512 region, the low number of counts at harder energies prohibit robust constraints on the SP contamination model, most importantly on the slope of the power-law component. This is a problem because uncertainties on this parameter will dramatically affect the derived diffuse emission spectral parameters. To circumvent this we used the full-field EPIC spectra (see Sect. 2.2), excluding point sources, and fitted these spectra in the 3–7 keV energy range. Because the SP contamination component should dominate at these energies, we can constrain the shape of the spectrum, which was then fixed in the fits to the inner NGC 1512 spectrum. We find that the residual SP contamination can be modelled as a power-law of photon index $\Gamma = 0.22$ for the EPIC-PN spectrum and $\Gamma = 0.35$ for the EPIC-MOS spectra.

3.4.2. Astrophysical background

The astrophysical background (APB) typically comprises four or fewer components (Snowden et al. 2008; Kuntz & Snowden 2010), namely the unabsorbed thermal emission from the local

[6] `http://heasarc.gsfc.nasa.gov/ftools/`
[7] http://www.atomdb.org/

hot bubble (LHB, $kT \sim 0.1$ keV), absorbed cool ($kT \sim 0.1$ keV) and warm ($kT \sim 0.25$ keV) thermal emission from the Galactic halo, and an absorbed power-law representing unresolved background cosmological sources ($\Gamma \sim 1.46$, Chen et al. 1997). All thermal components were fitted with the `vapec` (Smith et al. 2001) thermal plasma model in `XSPEC`. To model the absorption of the Galactic halo and cosmological background sources we used the photoelectric absorption model `phabs` in `XSPEC`. The value of the foreground hydrogen absorption column was fixed at 1×10^{20} cm^{-2} based on the Leiden/Argentine/Bonn (LAB) Survey of Galactic HI (Kalberla et al. 2005), determined using the HEASARC $N_{\rm H}$ Tool[8]. Because of this very low foreground absorption value, the LHB and cool Galactic halo emission are more or less indistinguishable in our spectral analysis energy range, which is why we treated them as a single component in the fits.

3.4.3. SWCX

Given the high level of residual SP contamination in our observation, we also considered whether SWCX emission is present in our spectra as well. An SWCX spectrum consists of emission lines corresponding to the ions in the solar wind. Unfortunately, these lines are also of great astrophysical importance and can affect the derived spectral parameters of the astrophysical source at issue. SWCX occurs in several regions of the solar system, but the most important in terms of *XMM-Newton* observations is caused by solar wind ions that interact with the Earth's magnetosheath (Robertson & Cravens 2003). There are two main influences on the level of SWCX contamination of a spectrum. First, because SWCX is generated by highly charged ions in the solar wind, flux enhancements of the solar wind naturally lead to a higher production of SWCX X-rays. Second, the viewing geometry of *XMM-Newton* with respect to the magnetosheath will affect the level of contamination, meaning that observations made with *XMM-Newton* through more of the magetosheath are subject to more contamination. Because of the orbit of *XMM-Newton* around Earth and that of Earth around the Sun, certain periods of the year are more susceptible to SWCX contamination, with the summer months being the worst affected (see Fig. 1 of Carter & Sembay 2008, for a nice illustration). Our observation of NGC 1512 with strong residual SP contamination was performed on June 16/17 2012 and therefor might be affected. The easiest way to identify SWCX contamination is to have multi-epoch observations of the same region of sky. We searched the *XMM-Newton* archives for an appropriate observation. Obs ID. 0501210701 (PI: M Ajello) was performed on July 7 2007, has an aimpoint $\sim 30'$ from the nucleus of NGC 1512, and was found to be effectively free of SP contamination. Using XMM-ESAS, we extracted spectra from the central $10'$ of this 'background' field and from all of the NGC 1512/1510 field (point sources and central diffuse emission region excluded) to characterise the APB and search for SWCX. Because we limited our *XMM-Newton* spectral analysis to > 0.4 keV, we obtained the *ROSAT* All-Sky Survey (RASS) spectrum from a 1°-2° annulus around NGC 1512 (using the HEASARC X-ray background tool[9]) to constrain the soft emission below 0.5 keV. We initially fitted the background field spectra with the RASS spectrum to constrain the local APB (see the black and red spectra in Fig. 4-left). We obtained a good fit to the data (χ^2_ν=1.05) with fit parameters in the expected ranges. Next we assumed that this background model represented the background of the NGC 1512/1510 observation and fixed the relevant background components in the model. The resulting fit to the spectra was very poor (χ^2_ν >2) with high residuals < 1 keV, which could be attributed to SWCX. Therefore, we added a series of Gaussian components to the model that represent the emission lines expected from SWCX (listed in the ESAS cookbook), namely C VI (0.46 keV), O VII (0.56 keV), O VIII (0.65 keV), O VIII (0.81 keV), Ne IX (0.92 keV), Ne IX (1.02 keV), and Mg XI (1.35 keV). The addition of these emission lines resulted in a substantially improved fit (χ^2_ν=1.11), which is shown in green in Fig. 4 (left) for comparison with the background field and RASS spectra, and alone in Fig. 4 (right) with the additive components of the spectral model highlighted. Based on these results, it is evident that the observation of NGC 1512/1510 is heavily contaminated by SWCX. While there may be some real NGC 1512 emission buried in this contamination, the level of SWCX prohibits any meaningful treatment. Accordingly, we considered only the central diffuse emission region for the subsequent analysis with the background components (APB, SWCX, and SPs) fixed appropriately.

3.4.4. Spectral fitting

We extracted EPIC-MOS and EPIC-PN spectra from the central region of diffuse emission in NGC 1512. The count statistics for each spectrum are relatively low, with EPIC-MOS spectra ~ 400 counts and EPIC-PN ~ 650 counts. Hence, we decided to fit only the EPIC-PN data because this spectrum is of the best statistical quality. While not completely satisfactory, it at least allowed us to obtain coarse estimates of the diffuse emission parameters, although more complex models (e.g., non-equilibrium ionisation components, metallicity enhancements) are beyond our grasp. We assumed that the soft emission in the central NGC 1512 region is thermal in origin. Therefore, we fitted the EPIC-PN spectrum with the fixed background components and a single thermal plasma model (`vapec` in `XSPEC`) with abundances set to those of NGC 1512 (0.65 solar, Koribalski & López-Sánchez 2009). Absorption components were included to represent the foreground Galactic column density and absorption due to material in NGC 1512. This second component consistently tended to zero and only an upper limit could be determined. However, we caution that the fit is not very sensitive to this parameter since the SWCX lines dominate the softer energies where the constraints on this parameter are determined. Thus, the resulting upper limit may be somewhat misleading. Comparing this upper limit with the determined $N_{\rm H}$ values of the compact sources in NGC 1512 (see Table 7), we see that the upper limit from the diffuse emission fit is an order of magnitude higher than that of all sources in the D_{25} ellipse of NGC 1512. The $N_{\rm H}$ values of the compact sources seem to point to a very low intrinsic absorption in the galaxy. The resulting spectral fit was statistically acceptable (χ^2_ν=0.93) with $kT = 0.66$ (0.28 – 0.89) keV and unabsorbed flux of 1.1×10^{-14} erg cm^{-2} s^{-1}. Because this flux is derived from diffuse emission regions with point sources masked, we corrected it for the excluded regions. Assuming that the average surface brightness of the detected diffuse emission holds across the point source regions, the resulting X-ray flux is $F_{\rm X,0.3-10\ keV} = 1.4 \times 10^{-14}$ erg cm^{-2} s^{-1}. This corresponds to an X-ray luminosity $L_{\rm X,0.3-10\ keV} = 1.5 \times 10^{38}$ erg s^{-1} at the distance of NGC 1512.

[8] `http://heasarc.gsfc.nasa.gov/cgi-bin/Tools/w3nh/w3nh.pl`

[9] `http://heasarc.gsfc.nasa.gov/cgi-bin/Tools/xraybg/xraybg.pl`

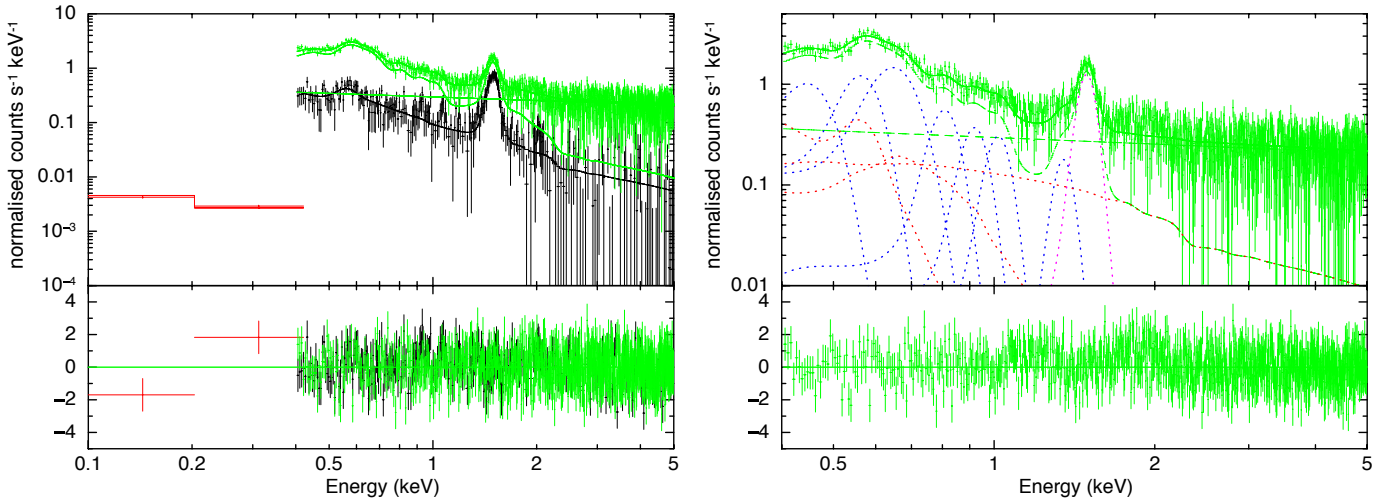

Fig. 4. *Left*: Various background spectra considered for our analysis. The black lines indicate the background field spectrum that was fitted simultaneously with the RASS background (shown in red) to constrain the emission components < 0.5 keV. This model was then used to fit the NGC 1512/1510 observational background (shown in green for comparison), which required additional components for SWCX contamination. *Right*: NGC 1512/1510 observational background. Additional model components are indicated with APB in red, fluorescence line in magenta, and SWCX lines in blue. The green dashed line that follows the data more closely represents the combined additive model, while the straight dashed black line represents the residual SP contamination. The addition of these two provides the total model indicated by the solid green line. In each panel, only EPIC-PN spectra are shown for clarity.

Table 4. Spectral fit results for the central diffuse emission in NGC 1512. See text for description of the model components.

Comp.	Parameter	Value
	Foreground Absorption	
phabs	$N_{\rm H}$ (10^{22} cm^{-2})	0.01 (fixed)[a]
vphabs	$N_{\rm H}$ (10^{22} cm^{-2})	0.00 (< 0.38))[b]
	NGC 1512 components	
vapec[c]	kT (keV)	0.66 (0.28–0.89)
	norm (10^{-6})	1.28 (0.84–1.76)
	$F_{\rm X,0.3-10\ keV}$ (10^{-14} erg cm^{-2} s^{-1})	1.4[d]
	$L_{\rm X,0.3-10\ keV}$ (10^{38} erg s^{-1})	1.5[d]
Fit statistic	χ^2_ν	0.93 (27 d.o.f.)

Notes. The APB, SWCX, and SP parameters are fixed according to the background results described in the text.
[(a)] Fixed to the Galactic column density from the Leiden/Argentine/Bonn (LAB) Survey of Galactic HI (Kalberla et al. 2005). [(b)] Abundances fixed to those of NGC 1512. Only an upper limit for $N_{\rm H}$ could be determined. We caution that this upper limit may be misleading as the fit is not very sensitive to the parameter (see text). [(c)] Abundances fixed to those of NGC 1512. [(d)] Values are de-absorbed.

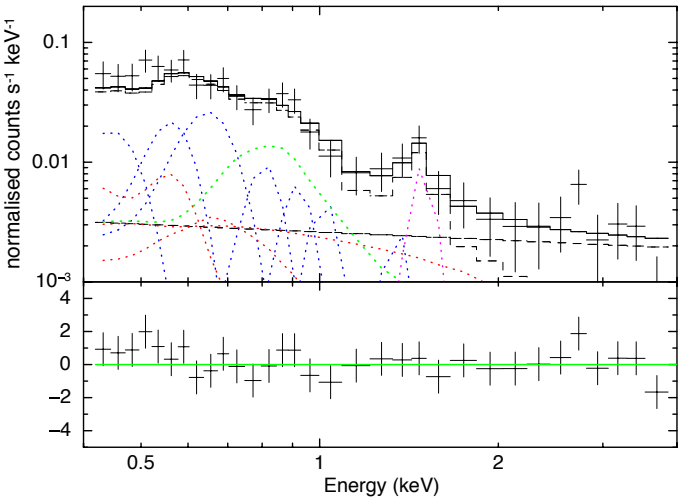

Fig. 5. Fit to the EPIC-PN spectrum of the central diffuse emission in NGC 1512. Additive model components are indicated with APB in red, fluorescence line in magenta, SWCX lines in blue, and source emission in green. Results of the source component are presented in Table 4. The black dashed line that follows the data more closely represents the combined additive model, while the straight dashed black line represents the residual SP contamination. The addition of these two provides the total model indicated by the solid black line.

4. Source classification

We compared the list of X-ray sources detected in the *XMM-Newton* observation with sources observed in other wavelengths to find the counterparts. To this purpose we used optical (USNO-B1, Monet et al. 2003; Muenster Red Sky Survey (MRSS), Ungruhe et al. 2003; Tycho-2 Catalogue (TYC), Høg et al. 2000), infrared (2MASS, Skrutskie et al. 2006), and radio (Sydney University Molonglo Sky Survey (SUMSS), Mauch et al. 2003) catalogues. We considered sources observed at different wavelengths to be associated if their positions were closer than the three times combined statistical errors. When an X-ray source had many optical counterparts, we only considered the brightest one within the error circle. This comparison allowed us to identify some of the *XMM-Newton* sources with sources previously classified in other wavelengths. When a previous classification was not available, we tried to classify the X-ray sources using their X-ray, optical, infrared, and radio properties.

For each X-ray source, possible optical, infrared, and radio counterparts are reported in Table B.2.

4.1. Foreground stars

The *XMM-Newton* field of view of NGC 1512/1510 is contaminated by stars belonging to our Galaxy. The X-ray spectra of foreground stars are somewhat softer than the X-ray spectra of other classes of sources. Moreover, their X-ray emission is usually expected to be $f_x \lesssim 10^{-1} f_{opt}$ (e.g. Krautter et al. 1999), where f_{opt} is the flux in the optical band. A useful tool to classify stars compares the observed X-ray-to-optical and X-ray-to-infrared flux ratios with the expected ones. For each X-ray source with optical or infrared counterparts, we calculated f_x/f_{opt} and f_x/f_{IR} with the equations of Maccacaro et al. (1988) and Lin et al. (2012):

$$\log_{10}(f_x/f_{opt}) = \log_{10}(f_x) + \frac{m_v}{2.5} + 5.37 \quad (2)$$

$$\log_{10}(f_x/f_{IR}) = \log_{10}(f_x) + \frac{m_{K_s}}{2.5} + 6.95\,, \quad (3)$$

where m_v is the visual magnitude that we obtained from the USNO-B1 red and blue magnitudes, assuming $m_v \approx (m_{red} + m_{blue})/2$ and m_{k_s} is the magnitude in the K_s−band from the 2MASS catalogue. Figure 6 shows $\log_{10}(f_x/f_{opt})$ over the hardness ratios HR_2 and HR_3. Foreground stars are expected to be in the regions of Fig. 6 with $\log_{10}(f_x/f_{opt}) \leq -1$ and, because of their soft X-ray spectra, $HR_2 \lesssim 0.3$ and $HR_3 \lesssim -0.4$ (Pietsch et al. 2004). Following the classification scheme derived by Lin et al. (2012), we also required $\log_{10}(f_x/f_{IR}) \leq -1$. In addition, we used optical and near-infrared magnitudes to classify foreground stars. They are expected to be brighter in R than background objects and with colors $B-R$ and $J-K$ overlapping the intrinsic colours of main sequence, giant and supergiant stars of our Galaxy showed in Fig. 7 with three lines (obtained from Johnson 1966) .

Another method to classify Galactic objects is based on proper motions. We used the proper motion measurements provided by the *PPMXL Catalog of positions and proper motions on the ICRS* (Roeser et al. 2010) or other catalogues of proper motions (e.g. the *Yale/San Juan Southern Proper Motion Catalog 4 (SPM4)* Girard et al. 2011 and *the Fourth U.S. Naval Observatory CCD Astrograph Catalog (UCAC4)* Zacharias et al. 2013).

From previous considerations we classified a source to be a foreground star when all these conditions were met:

- $\log_{10}(f_x/f_{opt}) \leq -1$;
- $\log_{10}(f_x/f_{IR}) \leq -1$;
- $HR_2 \lesssim 0.3$;
- $HR_3 \lesssim -0.4$;
- $J - K_s \lesssim 1.0$.

or:

- measurement of the proper motion provided by the PPMXL catalogue.

Six sources met these criteria, hence we classified them as foreground stars (Table 5). Four of them (No. 4, 9, 40, 89) show X-ray, optical, and infrared properties typical of normal stars. The remaining No. 13 and 94 have peculiar properties indicating the possible presence of an accreting companion star. In particular, both have a radio (ATCA) counterpart. Source No. 82 lies on the lines of intrinsic colours of stars in Fig. 7, but its HR_3 is too hard for a foreground star (see Fig. 6).

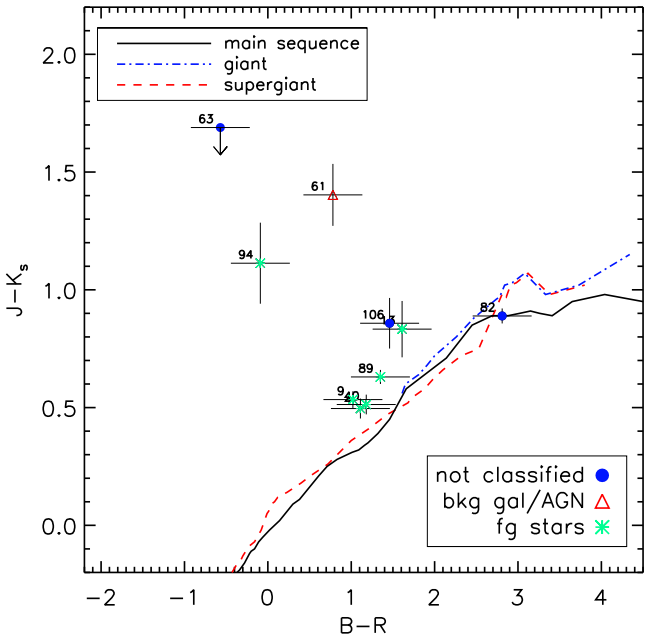

Fig. 7. Colour-colour diagram of *XMM-Newton* sources with optical (USNO-B1) and infrared (2MASS) counterparts.

A detailed discussion of the classification of the most interesting foreground stars is provided in Sect. A.1.

4.2. Background objects

Another class of sources included in the X-ray observations of nearby galaxies are the background objects: normal galaxies, AGNs, and galaxy clusters.

The identification of a background object in this work is based on SIMBAD and NED correlations. This allowed us to identify source No. 61 with a galaxy (MRSS 250-126782, Ungruhe et al. 2003, and 2MASX J04035631-4329046, 2 Micron All Sky Survey Extended objects, Skrutskie et al. 2006; see Table 6).

The existence of a radio counterpart and a hardness ratio of $HR_2 \geq -0.4$ (Pietsch et al. 2004) are indicative of an AGN. We found radio counterparts for the hard sources No. 23, 67, 71, 83, 98 (see Table 6 and Sect. A.2) and classified them as AGNs for the first time.

4.3. Sources in NGC 1512/1510

We detected 21 sources inside the D_{25} ellipses (NGC 1512: 8.9× 5.6 arcmin^2; NGC 1510: 1.3×0.7 arcmin^2; de Vaucouleurs et al. 1991) of NGC 1512 and NGC1510 or overlapping the outer galaxy arms detected by GALEX. These sources, with their positions, hardness ratios, fluxes and luminosities (assuming d = 9.5 Mpc) are listed in Table 8. The detection-limiting flux in the 0.2 − 12 keV energy band is $\sim 2.6 \times 10^{-15}$ erg cm^{-2} s^{-1} for sources inside the D_{25} ellipses. In Table 8 we did not include sources identified and classified as background objects or foreground stars. We included source No. 63, classified as quasi-stellar object (QSO) in the catalogue of Atlee & Gould (2007),

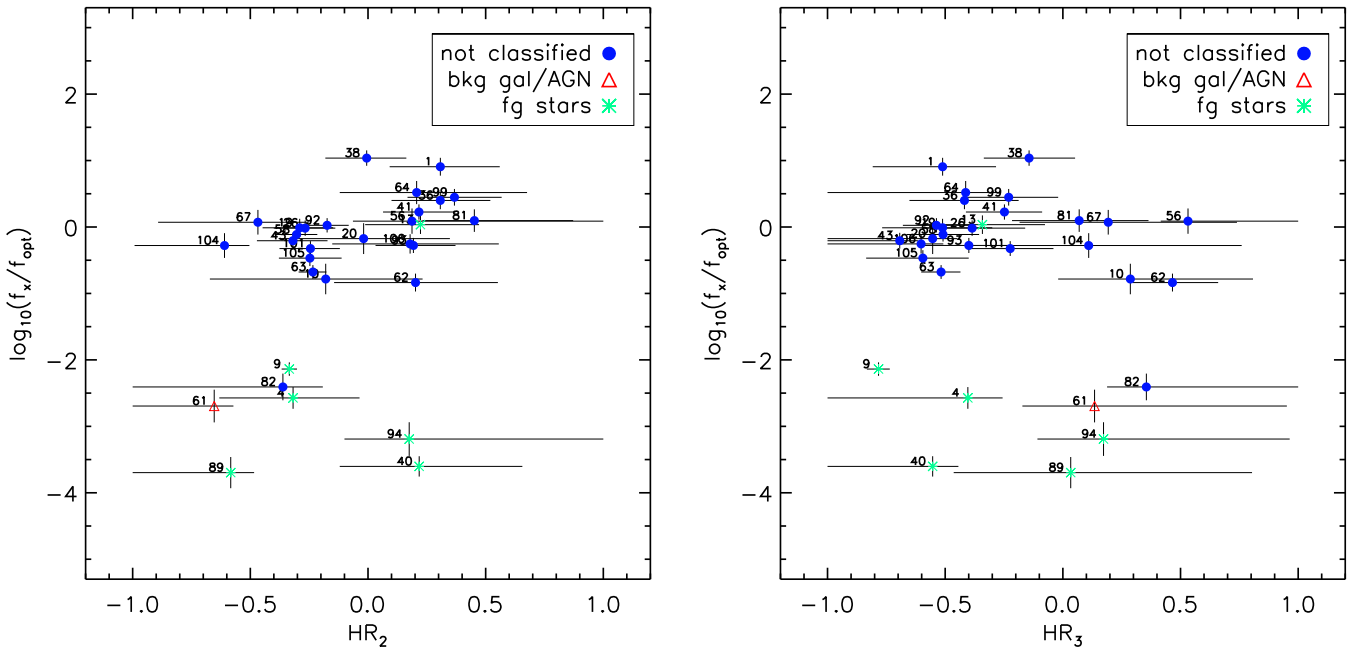

Fig. 6. Flux ratio $\log(f_x/f_{opt})$ over hardness ratios HR_2 and HR_3.

Table 5. X-ray sources classified as foreground star candidates and the associated optical counterparts. pmRA and pmDec are the proper motion of the star in milli-arcsec per year. Proper motion velocities are taken from the PPMXL catalogue.

No.	RA (J2000)	Dec (J2000)	USNO-B1	B mag.	R mag.	pmRA (mas yr^{-1})	pmDec (mas yr^{-1})
4	04 02 59.40	−43 32 23.6	0464-0031137	15.13	14.02		
9†*	04 03 07.15	−43 30 29.0	0464-0031154	12.61	11.59	−6.2 ± 1.8	−7.4 ± 1.8
13	04 03 12.96	−43 11 57.6	0468-0031995	21.25	19.64	85.4 ± 10.3	−49.8 ± 10.3
40†*	04 03 40.85	−43 28 57.1	0465-0031108	12.28	11.1	18.3 ± 1.7	−3.0 ± 1.7
89	04 04 31.49	−43 26 10.4	0465-0031223	12.69	11.34	12.5 ± 2.1	9.6 ± 2.1
94†	04 04 43.73	−43 25 22.9	0465-0031250	14.63	14.72	−16.3 ± 10.4	10.4 ± 10.4

Notes:
†: this star also has an independent proper motion measurement in the Yale/San Juan Southern Proper Motion Catalog 4 (SPM4) (Girard et al. 2011); *: this star also has an independent proper motion measurement in the Fourth U.S. Naval Observatory CCD Astrograph Catalog (UCAC4) (Zacharias et al. 2013).

Table 7. Best-fitting parameters of the X-ray spectra of sources No. 23, 54, and 63 (errors at 90% confidence level). The fluxes (erg cm^{-2} s^{-1}) have been calculated in the energy range 0.2 − 10 keV. Galactic absorption: $N_H = 10^{20}$ cm^{-2}.

No.	N_H (10^{21} cm^{-2})	Γ	kT (diskbb) (keV)	χ^2_ν (d.o.f.)† c-stat (d.o.f.)	goodness	F_x (0.2 − 10 keV)	unabs. F_x erg cm^{-2} s^{-1}
23	$2.8^{+0.9}_{-0.7}$	$3.6^{+0.5}_{-0.4}$		1.25 (31)		$6.9^{+6.1}_{-3.2} \times 10^{-14}$	$7.0^{+5.7}_{-3.4} \times 10^{-13}$
30	$\lesssim 0.1$		$0.66^{+0.17}_{-0.15}$	367.18 (442)	51.19%	$1.9^{+0.4}_{-0.4} \times 10^{-14}$	$1.7^{+0.4}_{-0.4} \times 10^{-14}$
33	$0.04^{+0.44}_{-0.04}$		$1.26^{+0.37}_{-0.30}$	248.92 (365)	2.97%	$2.7^{+0.7}_{-0.6} \times 10^{-14}$	$2.8^{+13.0}_{-1.8} \times 10^{-14}$
54	$\lesssim 0.2$	$1.4^{+0.4}_{-0.4}$	$0.28^{+0.03}_{-0.04}$	1.10 (65)		$8.8^{+0.9}_{-0.9} \times 10^{-14}$	$9.3^{+1.0}_{-0.8} \times 10^{-14}$
58	$0.02^{+0.26}_{-0.02}$	$2.0^{+0.3}_{-0.2}$		453.52 (546)	13.11%	$3.4^{+0.6}_{-0.5} \times 10^{-14}$	$1.6^{+2.1}_{-0.8} \times 10^{-13}$
63	$\lesssim 0.1$	$2.2^{+0.2}_{-0.1}$		0.90 (29)		$9.4^{+0.7}_{-1.1} \times 10^{-14}$	$1.0^{+0.2}_{-0.5} \times 10^{-13}$
92	$\lesssim 0.1$		$0.58^{+0.13}_{-0.10}$	321.24 (413)	23.16%	$4.5^{+0.8}_{-0.7} \times 10^{-14}$	$4.4^{+0.7}_{-0.7} \times 10^{-14}$

Notes:
† Reduced χ^2 and d.o.f. or Cash statistic, d.o.f. and percentage of realisations with statistic < c-stat

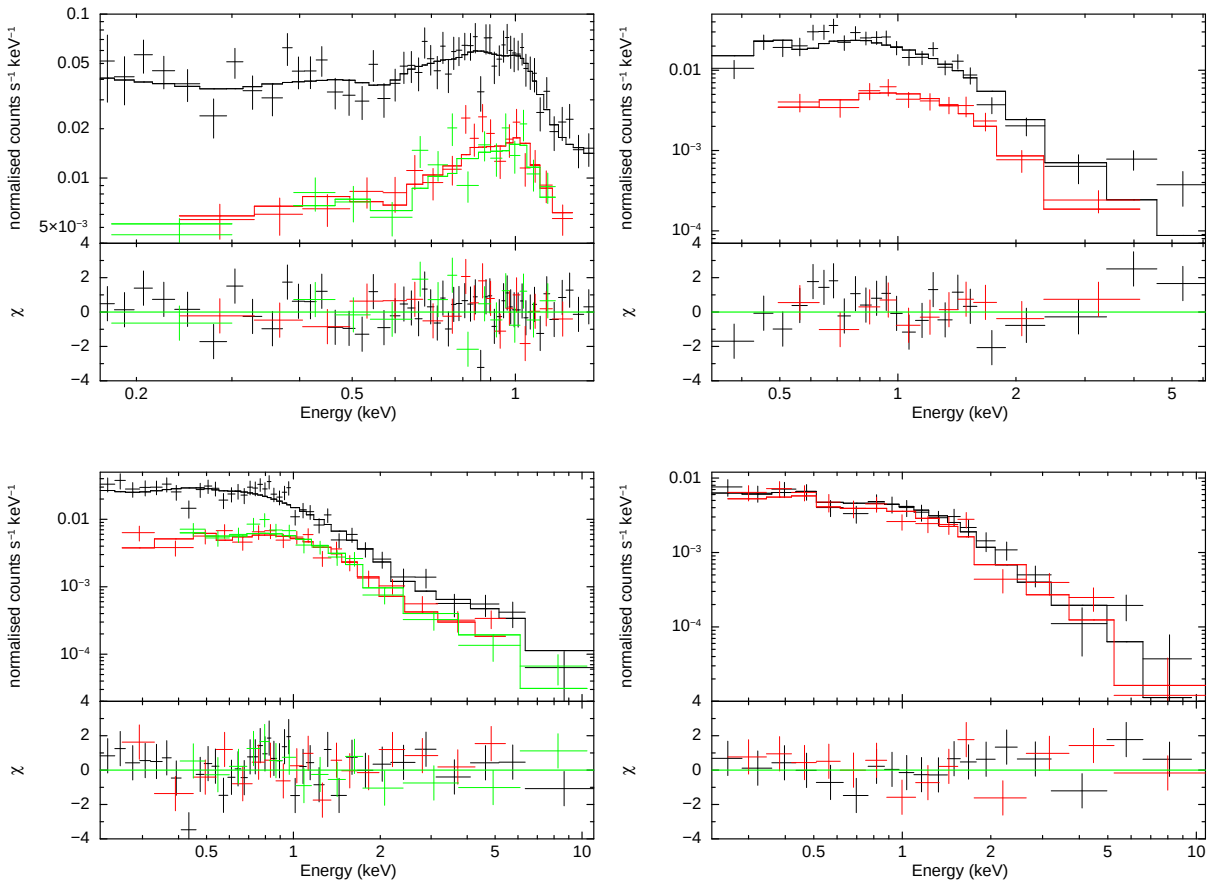

Fig. 8. EPIC counts spectra, together with residuals in units of standard deviations for sources No. 9 (top-left panel), No. 23 (top-right panel; PN: black; MOS2: red), No. 54 (bottom-left panel; PN: black; MOS1: red; MOS2: green), and No. 63 (bottom-right panel; MOS1: black; MOS2: red).

Table 6. X-ray sources identified and classified as galaxies or AGNs.

No.	*XMM-Newton* RA (J2000)	*XMM-Newton* Dec (J2000)	Counterpart Name or RA/Dec (J2000)	
Identifications:				
61	04 03 56.60	−43 29 05.0	2MASS J04035632-4329041	
Classification:				
23†	04 03 25.37	−43 17 22.0	04 03 25.54	−43 17 23.2
67†	04 04 08.90	−43 18 43.8	04 04 08.82	−43 18 42.3
71†	04 04 12.64	−43 22 30.7	SUMSS J040412-432235	
83†	04 04 22.57	−43 24 52.3	04 04 22.25	−43 24 52.1
98†	04 04 47.14	−43 22 03.5	04 04 46.77	−43 22 02.2

Notes:
† radio sources detected by ATCA

whose intermediate ultra-luminous X-ray source (ULX) nature cannot be ruled out (see Sect. 5.3). Sources No. 54 and 29 correspond to the nuclear regions of NGC 1512 and NGC 1510. The properties of source No. 54 are discussed in Sect. 5.1. The remaining 20 sources are discussed in Sects. 5.2 and 5.3.

5. Discussion

5.1. Nuclear source of NGC 1512 (XMMU J040354.2-432056)

Source No. 54 (XMMU J040354.2-432056) is the nuclear source of NGC 1512 and is the brightest source inside the D_{25} ellipse. Because of the relatively poor spatial resolution of *XMM-Newton*, we cannot study this region of NGC 1512 in detail, as the X-ray emission is expected to be produced by diffuse emission, unresolved point sources (dominated by XRBs), and a possible active nucleus with a low accretion rate in the galactic centre.

The 0.2 – 10 keV *XMM-Newton* light curve and the *Swift*/XRT measurements of the flux (see Table 3) show neither short- nor long-term variability. The source was bright enough to allow spectral analysis. We extracted PN, MOS1, and MOS2 spectra and fitted them simultaneously using different spectral models. The best-fit model (χ^2_ν = 1.08, 66 d.o.f.) is an absorbed power-law plus disc-blackbody, with a photon-index of $\Gamma = 1.4 \pm 0.4$, a temperature of $kT_{\rm in} = 0.28^{+0.03}_{-0.04}$ keV, and a luminosity of $L_{\rm x} = 1.00^{+0.11}_{-0.09} \times 10^{39}$ erg s^{-1} in the energy band 0.2 – 10 keV (Table 7; Fig. 8). The spectral parameters and the X-ray luminosity are typical of accreting intermediate-mass black holes (IMBHs; see e.g. Stobbart et al. 2006). We also obtained an acceptable fit (χ^2 = 0.90, 65 d.o.f.) with an absorbed power-law plus thermal component, `phabs(powerlaw+apec)`,

with $\Gamma = 2.10 \pm 0.11$ and $kT = 0.58^{+0.13}_{-0.22}$ keV. Although this spectral model overfits the data with a $\chi^2 = 0.90$, it describes the expected X-ray emission from the unresolved nuclear region of a galaxy better, where a fraction of the X-ray emission is produced by point sources and the remaining emission comes from interstellar gas. The power-law photon index obtained with this fit is compatible with the spectral emission from an active nucleus with a very low accretion rate[10], or with the spectral emission from XRBs.

5.2. Source No. 63 (XMMU J040400.9-432319)

The second-brightest source in the D_{25} of NGC 1512 is source No. 63. It coincides with the infrared source 2MASS J04040093-4323175 and the optical source USNO-B1 0466-0031610. We extracted the MOS1 and MOS2 spectra (the position of the source was close to a gap in PN) and found that an absorbed power-law provides an acceptable fit (see Table 7 and Fig. 8). No. 63 does not show any significant variability in the *XMM-Newton* and *Swift* observations (Table 3). Atlee & Gould (2007) classified the optical counterpart of No. 63 as a QSO candidate according to the selection criteria based on optical (USNO A2.0, Monet 1998) and UV (GALEX Release Two) properties. The catalogue of Atlee & Gould (2007) provides a probability of 36% that this source is a QSO candidate. Therefore we investigated other possible classifications. A comparison between the optical/infrared colours and the optical luminosity from USNO B1 and 2MASS catalogues with the stellar spectral flux library of Pickles (1998) shows that No. 63 cannot be a foreground star. If No. 63 belongs to NGC 1512, its 0.5 – 10 keV luminosity would be $8 - 13 \times 10^{38}$ erg s^{-1}, exceeding the Eddington limit of an accreting neutron star and compatible with an accreting black hole with an X-ray luminosity lying just below the conventional luminosity threshold of $\sim 10^{39}$ erg s^{-1} of ULXs.

5.3. Other sources in NGC 1512/1510

The 0.2 – 12 keV fluxes of the remaining 19 sources range from $\sim 3.4 \times 10^{-15}$ erg cm^{-2} s^{-1} to $\sim 9.6 \times 10^{-14}$ erg cm^{-2} s^{-1} ($3.7 \times 10^{37} \lesssim L_x \lesssim 10^{39}$ erg s^{-1}, assuming $d = 9.5$ Mpc). These sources are too faint to perform a spectral analysis. Therefore we used the hardness ratios to outline their X-ray properties. Figure 3 shows the hardness ratios of sources in NGC 1512/1510 with uncertainties less than 0.3 and a grid of hardness ratios calculated for different spectral models (Sect. 3.2). The entire sample of sources plotted in Fig. 3 shows hardness ratios compatible with power-law or disc-blackbody models, indicating that they might either be accreting compact objects in NGC 1512/1510 or background objects.

XMM-Newton detected 13 non-nuclear sources inside the D_{25} ellipse of NGC 1512 in the energy band 0.2 – 12 keV. Based on the spectral emission properties emerging from the hardness ratios, they can be either XRBs or AGNs. Assuming that AGNs are uniformly distributed in the sky, their number within the D_{25} ellipse of NGC 1512 can be derived statistically using the 0.5 – 2 keV and 2 – 10 keV $\log N - \log S$ AGN distributions of Cappelluti et al. (2009). The $\log N - \log S$ in the energy range 2 – 10 keV is almost unaffected by the incompleteness effect produced by the absorption. In contrast, this effect is present in the energy range 0.5 – 2 keV. We accounted for NGC 1512 absorption in the 0.5–2 keV $\log N - \log S$ by assuming that the total column density through the galactic disc (along the directions perpendicular to the galactic plane) is 5×10^{20} cm^{-2}, in agreement with the hydrogen distribution in the direction perpendicular to the Galactic plane of the Milky Way (Kalberla & Kerp 2009). Then, assuming that the spectral emission of AGNs in 0.5 – 2 keV is described by a power-law with photon index $\Gamma = 2$ (see Cappelluti et al. 2009 and references therein), we found that AGNs beyond NGC 1512 detected with a flux $\geq 1.1 \times 10^{-15}$ erg cm^{-2} s^{-1} would have fluxes $\geq 1.2 \times 10^{-15}$ erg cm^{-2} s^{-1} if they were not absorbed by NGC 1512. We found that 7 ± 0.5 AGNs are expected in the D_{25} ellipse of NGC 1512 in the energy range 0.5 – 2 keV with observed fluxes $\geq 1.1 \times 10^{-15}$ erg cm^{-2} s^{-1} and 6.9 ± 0.5 AGNs in the energy range 2 – 10 keV with observed fluxes higher than the 2 – 10 keV limiting flux 4.3×10^{-15} erg cm^{-2} s^{-1}. The numbers derived above can be compared with the numbers of sources detected by *XMM-Newton* with a higher detection likelihood than 6 in the energy bands 0.5 – 2 keV and 2 – 10 keV, within the D_{25} ellipse of NGC 1512. To accomplish this, we corrected the number of X-ray sources for the incompleteness effect. It consists of an underestimation of the number of sources detected in the surveyed area caused by the non-uniformity of the sensitivity of the EPIC instruments across the field of view. We corrected the number of X-ray sources in the D_{25} region as follows: we first created the combined sensitivity maps of the three EPIC instruments in the energy bands of 0.5 – 2 keV and 2 – 10 keV with the SAS task `esensmap`. We excluded a circular region centred on the nuclear region of NGC 1512 with radius 12 arcsec from this analysis, where the relatively poor spatial resolution of EPIC in a crowded region causes source confusion effects. $A_{\rm tot}$ is the area of the sky surveyed by EPIC. We used the resulting sensitivity maps to calculate the fraction of surveyed area

[10] Photon indices in the range of $\Gamma \sim 1.5 - 2.5$ have been measured in different AGNs (Ishibashi & Courvoisier 2010 and references therein).

Table 8. *XMM-Newton* sources within the D_{25} ellipses of NGC 1512 and NGC 1510.

No.	RA (J2000)	Dec (J2000)	Flux (0.2 – 12 keV) erg cm^{-2} s^{-1}	Luminosity (0.2 – 12 keV) erg s^{-1}
24[1]	04 03 25.76	−43 23 10.0	$(1.7 \pm 0.5) \times 10^{-14}$	$(1.8 \pm 0.5) \times 10^{38}$
28	04 03 32.12	−43 21 39.2	$(1.9 \pm 0.2) \times 10^{-14}$	$(2.1 \pm 0.2) \times 10^{38}$
29[2]	04 03 32.71	−43 24 01.7	$(2.3 \pm 0.6) \times 10^{-14}$	$(2.5 \pm 0.6) \times 10^{38}$
42	04 03 42.10	−43 18 38.5	$(8.4 \pm 3.4) \times 10^{-15}$	$(9.1 \pm 3.7) \times 10^{37}$
43	04 03 42.40	−43 19 58.9	$(1.6 \pm 0.4) \times 10^{-14}$	$(1.7 \pm 0.4) \times 10^{38}$
44	04 03 42.72	−43 23 17.1	$(1.1 \pm 0.3) \times 10^{-14}$	$(1.2 \pm 0.3) \times 10^{38}$
45	04 03 42.90	−43 20 50.2	$(5.2 \pm 2.7) \times 10^{-15}$	$(5.6 \pm 2.9) \times 10^{37}$
51	04 03 50.86	−43 22 04.9	$(5.1 \pm 2.5) \times 10^{-15}$	$(5.5 \pm 2.7) \times 10^{37}$
53	04 03 52.76	−43 20 59.0	$(4.3 \pm 3.2) \times 10^{-15}$	$(4.6 \pm 3.4) \times 10^{37}$
54[3]	04 03 54.26	−43 20 56.7	$(9.8 \pm 0.6) \times 10^{-14}$	$(10.6 \pm 0.6) \times 10^{38}$
55	04 03 54.30	−43 18 53.0	$(7.6 \pm 2.6) \times 10^{-15}$	$(8.2 \pm 2.8) \times 10^{37}$
57	04 03 54.79	−43 22 24.5	$(6.7 \pm 5.0) \times 10^{-15}$	$(7.2 \pm 5.4) \times 10^{37}$
59[1]	04 03 56.14	−43 17 20.7	$(1.6 \pm 0.3) \times 10^{-14}$	$(1.7 \pm 0.3) \times 10^{38}$
62	04 03 58.34	−43 22 46.0	$(1.5 \pm 0.5) \times 10^{-14}$	$(1.6 \pm 0.5) \times 10^{38}$
63[4]	04 04 00.99	−43 23 19.0	$(9.6 \pm 0.7) \times 10^{-14}$	$(10.4 \pm 0.8) \times 10^{38}$
67	04 04 08.90	−43 18 43.8	$(3.4 \pm 1.7) \times 10^{-15}$	$(3.7 \pm 1.8) \times 10^{37}$
69	04 04 11.17	−43 19 57.7	$(1.6 \pm 0.4) \times 10^{-14}$	$(1.7 \pm 0.4) \times 10^{38}$
73[1]	04 04 14.97	−43 22 57.6	$(1.6 \pm 0.5) \times 10^{-14}$	$(1.7 \pm 0.5) \times 10^{38}$
74[1]	04 04 15.17	−43 22 34.3	$(4.1 \pm 3.4) \times 10^{-15}$	$(4.4 \pm 3.6) \times 10^{37}$
75[1]	04 04 15.21	−43 24 09.8	$(4.0 \pm 3.9) \times 10^{-15}$	$(4.3 \pm 4.2) \times 10^{37}$
90[1]	04 04 35.29	−43 20 06.7	$(8.5 \pm 7.0) \times 10^{-15}$	$(9.2 \pm 7.5) \times 10^{37}$

Notes: [1] outside of D_{25} but overlapping outer galaxy arms of GALEX observation; [2] nuclear region of NGC 1510; [3] nuclear region of NGC 1512; [4] QSO or intermediate ULX;

$\Omega(F_i)/A_{\rm tot}$, over which sources with a given flux F_i can be detected. Then, we used this factor to correct the total number of detected sources for each of the two energy bands considered for incompleteness with the formula $N = \sum_{i=1}^{N_{\rm d}} A_{\rm tot}/\Omega(F_i)$, where $N_{\rm d}$ is the number of detected sources and N is the number of sources corrected for incompleteness. We found seven sources with a flux higher than 1.1×10^{-15} erg cm^{-2} s^{-1} in the energy range of $0.5 - 2$ keV and nine sources with a flux higher than 4.3×10^{-15} erg cm^{-2} s^{-1} in the energy range $2 - 10$ keV. From a simple comparison we find that the number of expected AGNs calculated above agrees; these numbers are slightly lower than the number of X-ray sources observed by *XMM-Newton* and corrected for incompleteness, which means that they indicate a small population of XRBs in NGC 1512.

Since the number of HMXBs and LMXBs in nearby galaxies depends on the SFR and the stellar mass content, respectively (see e.g. Grimm et al. 2003; Gilfanov 2004), we obtained a rough estimate of the expected number of HMXBs and LMXBs in the D_{25} ellipse of NGC 1512 above the limiting flux of 4.3×10^{-15} erg cm^{-2} s^{-1} in the energy range of $2 - 10$ keV. Using the $N_{\rm HMXB} - SFR$ relation of Mineo et al. (2012a) (eq. 18) and $SFR \sim 0.2$ M$_\odot$ yr^{-1} (Koribalski & López-Sánchez 2009) we found $N_{\rm HMXB} \approx 1$. The number of LMXBs depends on the stellar mass M_* of a galaxy. We obtained $M_* \approx 10^{10}$ M$_\odot$ using the relation between the mass-to-light ratio M_*/L_K and the $B-V$ optical colour of Bell & de Jong (2001) ($\log[M_*/L_{\rm K}] = -0.692 + 0.652[B-V]$), the extinction-corrected total extrapolated magnitude K_s from the 2MASS redshift catalogue (Huchra et al. 2012), and the extinction-corrected $B-V$ optical colour from de Vaucouleurs et al. (1991) RC3 catalogue. Using the X-ray luminosity function calculated by Gilfanov (2004) (eq. 8), we obtained $N_{\rm LMXB} \approx 4$ in NGC 1512. The sum of the number of HMXBs and LMXBs obtained from SFR and M_* measurements and the number of expected AGNs agree with the number of X-ray sources observed by *XMM-Newton* within the D_{25} ellipse of NGC 1512.

5.4. Diffuse emission

We have detected a soft X-ray emitting component that is located in the ring of NGC 1512. Assuming a thermal plasma model for the emission yields a temperature of $kT = 0.66\,(0.28-0.89)$ keV. Typically, thermal emission from spiral galaxies exhibits a two-temperature spectrum with cool and hot components of $kT_{\rm cool} \sim 0.2$ keV and $kT_{\rm hot} \sim 0.7$ keV. For example, this two temperature model has been observed in M101 (Kuntz et al. 2003), M81 (Page et al. 2003), and in the barred-spirals NGC 6946 (Schlegel et al. 2003) and NGC 1672 (Jenkins et al. 2011). The temperature of our best-fit spectral model to the inner NGC 1512 spectrum agrees with the hotter component expected for spiral galaxies. We suspect that, because of the poor count statistics and significant contamination of our spectra, we simply lack the sensitivity to detect the expected soft component. Accordingly, we considered only the detected hot component but caution that it may not represent the underlying X-ray emission from the centre of NGC 1512. The detected emission may not be truly diffuse in origin. Unresolved discrete sources can contribute to the apparently diffuse source and must therefore be quantified.

5.4.1. Unresolved HMXBs

Typically, one can separate the unresolved discrete sources into contributions from objects associated with the young (HMXBs) and older (LMXBs; cataclysmic variables, CVs; and coronally active binaries, ABs) stellar populations in the region. Koribalski & López-Sánchez (2009) determined the ages of the UV-bright stellar populations in the nuclear region and ring of NGC 1512 and found ages > 130 Myr. Therefore, it is unlikely that any HMXBs are located in the central regions because they are associated with younger stellar populations with ages < 100 Myr.

5.4.2. Unresolved weak sources

Objects associated with the older stellar population are much more likely to contribute. Revnivtsev et al. (2007, 2008) demonstrated that the X-ray luminosity per unit stellar mass due to the weak X-ray sources (CVs and ABs) associated with the old stellar population in the solar vicinity (Sazonov et al. 2006) is compatible with that observed in other galaxies. Hence, we can determine the expected X-ray luminosity from the unresolved CVs and ABs using the mass or, equivalently, luminosity of the stellar population, which can be estimated using NIR data (see also Sect. 5.3). We determined the combined K_s-band luminosity of the central region of NGC 1512 using the 2MASS Large Galaxy Atlas (Jarrett et al. 2003, see Fig. 2 right). Conveniently, the isophotal K_s-band magnitude in the atlas is representative of the central region with $K_s = 7.7$. Converting this into a luminosity gives $L_{K_s} = 2.1 \times 10^9$ L$_\odot$. We then used the relation $L_{\rm X,0.5-2\ keV}/L_{K_s} = (5.9 \pm 2.5) \times 10^{27}$ erg s^{-1} $L_{K_s,{\rm L}_\odot}^{-1}$ (Revnivtsev et al. 2008) and adjusted for the X-ray energy range using their emission model and the WebPIMMS[11] tool to determine an expected contribution to the X-ray luminosity of $L_{\rm X,\ 0.3-10\ keV} = (1.9 \pm 0.8) \times 10^{37}$ erg s^{-1}.

5.4.3. Unresolved LMXBs

Unresolved LMXBs associated with the old stellar population can also contribute to the apparently diffuse emission. Since the number of LMXBs in a stellar population is related to the total mass (Gilfanov 2004), we estimated the X-ray luminosity of LMXBs below the detection threshold using the total stellar mass in the central region. Using the method outlined in Sect. 5.3 with the combined K_s-band magnitude of the stellar population, we estimated the total stellar mass in the central region to be $\sim 1.3 \times 10^9$ M$_\odot$. We then used Equation 11 of Gilfanov (2004) to estimate the number of LMXBs with $L_{\rm X} > 10^{37}$ erg s^1 and their combined luminosity to be ~ 2 and 1.0×10^{38} erg s^{-1}, respectively. As stated by Gilfanov (2004), this X-ray luminosity is related to the total $L_{\rm X}$ due to LMXBs through a correction factor of ≈ 1.1. Thus, the total LMXB population in the central region contributes $L_{\rm X} = 1.1 \times 10^{38}$ erg s^1. In addition to the nuclear source, there are two X-ray sources located in the interior region (see Fig. 1). The X-ray colours of these sources suggest that they are either XRBs or AGN, namely No. 51 and No. 53 (see Sect. 5.3). The stellar mass in the central region suggests that probably about two sources with $L_{\rm X} > 10^{37}$ erg s^1 are present. Since our source detection sensitivity is $\gtrsim 10^{37}$ erg s^1, No. 51 and No. 53 might be expected to be LMXBs. If that is the case, their combined $L_{\rm X} = (9.6 \pm 4.3) \times 10^{37}$ erg s^1, which is similar to the total emission expected from the LMXB population. This means that if these are indeed LMXBs, the $L_{\rm X}$ due to unresolved LMXBs is $< 5.7 \times 10^{37}$ erg s^1, with the upper limit being about half of the

[11] Available at `https://heasarc.gsfc.nasa.gov/Tools/w3pimms.html`

observed L_X in the central region.

5.4.4. Emission from the interstellar gas

With these unresolved source contributions in mind, we re-ran our spectral fits, this time including spectral components representing the unresolved discrete sources, to determine the plasma temperature and luminosity of the diffuse emission. We fixed the normalisations of these additional components so that they represented the upper limits of their luminosity contribution. For the CVs and ABs we used the model of Revnivtsev et al. (2008), a combination of a thermal plasma (`mekal` in `XSPEC`) with solar abundance and $kT = 0.5$ keV, and a power-law with photon index $\Gamma = 1.9$. For the LMXBs, we used a power-law model with photon index $\Gamma = 1.5$, typical of LMXBs (Soria & Wu 2003). The resulting plasma temperature for the truly diffuse emission is $kT = 0.68\ (0.31 - 0.87)$ keV and $L_{\mathrm{X,0.3-10\ keV}} = 1.3 \times 10^{38}$ erg s^{-1}. Mineo et al. (2012b) determined from a sample of nearby star-forming galaxies that the 0.5 – 2 keV luminosity of diffuse X-ray emission from the ISM is linearly correlated with the SFR of that galaxy as $L_{X,0.5-2\ \mathrm{keV}}(\mathrm{erg\ s^{-1}}) \approx (8.3 \pm 0.1) \times 10^{38} \mathrm{SFR\ (M_\odot yr^{-1})}$. Because the SFR of NGC 1512 is 0.22 M$_\odot$ yr^{-1} (Koribalski & López-Sánchez 2009), we expect $L_{\mathrm{X,0.5-2\ keV}}$ to be $\sim 2 \times 10^{38}$ erg s^{-1}. The observed $L_{\mathrm{X,0.5-2\ keV}}$ was found to be $\sim 1 \times 10^{38}$ erg s^{-1}, which is largely consistent with the relation of Mineo et al. (2012b). An explanation of the slight discrepancy may be the non-detection of the cooler ISM component, typically observed in star-forming galaxies, because of the sensitivity of our observation (see Sect. 5.4).

In the inner regions of spiral galaxies, there are three possible sources of a hot X-ray emitting gas: stellar winds and supernova remnants associated with the older stellar population, superwinds driven by active star formation, and an AGN (Tyler et al. 2004). Since the youngest stellar population in the inner NGC 1512 region is of intermediate age (~ 130 Myr), it is unlikely that a superwind is being driven as the massive stellar population has been exhausted. Similarly, the absence of an AGN in NGC 1512 naturally rules out this possible source. Thus, the hot gas is most likely being produced by supernovae from the older stellar population, that is, the supernovae currently feeding the hot gas are Type Ia remnants because there is no young stellar population (< 100 Myr) capable of producing core-collapse (CC) explosions. However, in the past the contribution from CC remnants most likely dominated the energy input because of the intense star formation in the ring and nuclear region of NGC 1512 caused by the interaction with NGC 1510, very likely around ~ 400 Myr ago (Koribalski & López-Sánchez 2009). The combined effect of the massive stellar winds and supernovae may even have driven a superwind, that blew hot gas out along the poles of the galaxy into the halo, entrained and shocked cooler gas in the disc and halo, and produced X-rays (e.g., Strickland & Heckman 2009). If the radiative cooling time were long enough, some contribution from this earlier epoch would be expected. Spectral signatures of a Type Ia origin would be evident as enhanced Fe lines in the spectrum. However, our spectra lack the count statistics to identify such a signature.

We can estimate some constraints on the physical parameters of the hot diffuse gas based on the results from our spectral fits. The normalisation of the thermal plasma model (K) representing the diffuse component can be related to the emission measure through

$$K = \frac{10^{-14}}{4\pi D^2} n_e n_{\mathrm{H}} V. \quad (4)$$

For a thermal plasma with 0.65 solar abundance, as is the case for NGC 1512, $n_e/n_{\mathrm{H}} \sim 1.2$. $V = Ah$, where A is the area of the extraction region in cm and h is the height of the emitting region. We scaled the h term to units of kpc to allow a direct comparison of our results with other works. We also introduced a volume filling factor f to account for the distribution of hot gas in the volume V. Equation 4 can now be written

$$n_e^2 = 2.7 \times 10^{-8} \frac{K 4\pi D^2}{A f h_{\mathrm{kpc}}} \mathrm{cm}^{-6}. \quad (5)$$

From our elliptical extraction region with semi-major and semi-minor axes of ~ 1.8′ and ~ 1.4′ (corresponding to ~ 4.9 kpc and ~ 3.8 kpc at the distance of NGC 1512), we determined A to be $\sim 5.5 \times 10^{44}$ cm^2. Solving Equation 5 with these values gives $n_e = (0.001 - 0.002) f^{-1/2} h_{\mathrm{kpc}}^{-1/2}$ cm^{-3}. Using this determined electron density and the best-fit plasma temperature, we also calculated the radiative cooling time (t_{cool}) of the gas as

$$t_{\mathrm{cool}} \sim \frac{3kT}{\Lambda n_e}, \quad (6)$$

with $\Lambda \sim 2 \times 10^{-23}$ erg cm^{-3} s^{-1} (Sutherland & Dopita 1993). This yields $t_{\mathrm{cool}} \sim 10^{10} f^{1/2} h_{\mathrm{kpc}}^{1/2}$ yr. The determined values of n_e and t_{cool} are very low and high, respectively, compared with those determined for the central regions of other galaxies. Tyler et al. (2004) determined n_e to be in the range $0.016 - 0.11 f^{-1/2} h_{\mathrm{kpc}}^{-1/2}$ cm^{-3} for their sample of spiral galaxies without an AGN. Their higher gas densities naturally lead to lower radiative cooling times $\sim 10^7 f^{1/2} h_{\mathrm{kpc}}^{1/2}$ yr. A possible explanation is that the bar in NGC 1512 may play some significant role since bars are known to drive gas from the disk to the nuclear regions of a galaxy, fuelling star formation, and feeding an AGN, if present (Shlosman et al. 1990). Therefore, this dynamic system might have disrupted the hot gas content in the inner region of NGC 1512, resulting in the low electron density we observe. For the moment, this is just a suggestion because our data do not allow for a more detailed analysis. Only deeper (and/or less contaminated) X-ray observations with *Chandra* or *XMM-Newton* will allow us to properly characterise the diffuse X-ray emission and address this question.

6. Summary

For the first time, we presented a study of the X-ray source populations and diffuse emission in the *XMM-Newton* field of view of the galaxy pair NGC 1512 and NGC 1510. We performed a source detection and obtained a catalogue containing 106 sources detected in the energy range of 0.2 – 12 keV, 15 within the D_{25} ellipses of NGC 1512 and NGC 1510, and about six sources in the extended arms of the galaxy pair. Based on the X-ray spectral analysis, Bayesian hardness ratios, X-ray variability (for which we also made use of archival *Swift*/XRT data), cross-correlations with catalogues in other wavelengths, and the 20-cm radio maps of ATCA, we identified counterparts for 37 sources, six of which were identified or classified as background objects and six as foreground stars. We discussed the nature of source No. 63 (XMMU J040400.9-432319), previously classified as a QSO (Atlee & Gould 2007). We have shown that its

properties are also consistent with an accreting black-hole in the galactic disc of NGC 1512.

We showed that the number of HMXBs and LMXBs obtained from measurement of the star formation rate and total mass of NGC 1512 is consistent with the number of X-ray sources observed within the D_{25} ellipse of NGC 1512, after taking into account the contribution of background AGNs.

We detected diffuse X-ray emission from the interior region of NGC 1512 with a plasma temperature $kT = 0.68$ (0.31 – 0.87) keV and a 0.3–10 keV X-ray luminosity of 1.3×10^{38} erg s^{-1}, after correcting for unresolved discrete sources. While the X-ray emission is most likely due to present and/or past stellar winds and supernovae, the derived electron densities and radiative cooling times seem to low and high, respectively, compared with those of other spiral galaxies.

Acknowledgements. This research is funded by the BMWi/DLR grant FKZ 50 OR 1209. MS and LD acknowledge support by the Deutsche Forschungsgemeinschaft through the Emmy Noether Research Grant SA 2131/1-1. This work is partially supported by the Bundesministerium für Wirtschaft und Technologie through the Deutsches Zentrum für Luft- und Raumfahrt (Grant FKZ 50 OG 1301). This research has made use of the SIMBAD database, operated at CDS, Strasbourg, France, and of the NASA/IPAC Extragalactic Database (NED), which is operated by the Jet Propulsion Laboratory, California Institute of Technology, under contract with the National Aeronautics and Space Administration. This research has made use of the VizieR catalogue access tool, CDS, Strasbourg, France. The original description of the VizieR service was published in Ochsenbein et al. (2000). This research has made use of data, software and web tools obtained from NASA's High Energy Astrophysics Science Archive Research Center (HEASARC), a service of Goddard Space Flight Center and the Smithsonian Astrophysical Observatory. This publication has made use of data products from the Two Micron All Sky Survey, which is a joint project of the University of Massachusetts and the Infrared Processing and Analysis Center, funded by the National Aeronautics and Space Administration and the National Science Foundation. This research has made use of SAOImage DS9, developed by Smithsonian Astrophysical Observatory. This work made use of the XMM-Newton Extended Source Analysis Software.

References

Arnaud, K. A. 1996a, in Astronomical Society of the Pacific Conference Series, Vol. 101, Astronomical Data Analysis Software and Systems V, ed. G. H. Jacoby & J. Barnes, 17
Arnaud, K. A. 1996b, in Astronomical Society of the Pacific Conference Series, Vol. 101, Astronomical Data Analysis Software and Systems V, ed. G. H. Jacoby & J. Barnes, 17
Atlee, D. W. & Gould, A. 2007, ApJ, 664, 53
Balucinska-Church, M. & McCammon, D. 1992, ApJ, 400, 699
Bauer, M., Pietsch, W., Trinchieri, G., et al. 2008, A&A, 489, 1029
Bell, E. F. & de Jong, R. S. 2001, ApJ, 550, 212
Buccheri, R., Bennett, K., Bignami, G. F., et al. 1983, A&A, 128, 245
Burrows, D. N., Hill, J. E., Nousek, J. A., et al. 2005, Space Sci. Rev., 120, 165
Cappelluti, N., Brusa, M., Hasinger, G., et al. 2009, A&A, 497, 635
Carkner, L., Mamajek, E., Feigelson, E., et al. 1997, ApJ, 490, 735
Carpano, S., Wilms, J., Schirmer, M., & Kendziorra, E. 2005, A&A, 443, 103
Carter, J. A. & Sembay, S. 2008, A&A, 489, 837
Cash, W. 1979, ApJ, 228, 939
Chen, L.-W., Fabian, A. C., & Gendreau, K. C. 1997, MNRAS, 285, 449
Cruddace, R. G., Hasinger, G. R., & Schmitt, J. H. 1988, in European Southern Observatory Conference and Workshop Proceedings, Vol. 28, European Southern Observatory Conference and Workshop Proceedings, ed. F. Murtagh, A. Heck, & P. Benvenuti, 177–182
Cutri, R. M., Skrutskie, M. F., van Dyk, S., et al. 2003, VizieR Online Data Catalog, 2246, 0
De Luca, A. & Molendi, S. 2004, A&A, 419, 837
de Vaucouleurs, G., de Vaucouleurs, A., Corwin, Jr., H. G., et al. 1991, Third Reference Catalogue of Bright Galaxies. Volume I: Explanations and references. Volume II: Data for galaxies between 0^h and 12^h. Volume III: Data for galaxies between 12^h and 24^h.
Di Stefano, R. & Kong, A. K. H. 2003, ApJ, 592, 884
Favata, F. 1998, in Astronomical Society of the Pacific Conference Series, Vol. 154, Cool Stars, Stellar Systems, and the Sun, ed. R. A. Donahue & J. A. Bookbinder, 511
Freyberg, M. J., Briel, U. G., Dennerl, K., et al. 2004, in Society of Photo-Optical Instrumentation Engineers (SPIE) Conference Series, Vol. 5165, Society of Photo-Optical Instrumentation Engineers (SPIE) Conference Series, ed. K. A. Flanagan & O. H. W. Siegmund, 112–122
Gehrels, N., Chincarini, G., Giommi, P., et al. 2004, ApJ, 611, 1005
Getman, K. V., Feigelson, E. D., Broos, P. S., Micela, G., & Garmire, G. P. 2008, ApJ, 688, 418
Gilfanov, M. 2004, MNRAS, 349, 146
Girard, T. M., van Altena, W. F., Zacharias, N., et al. 2011, AJ, 142, 15
Grimm, H.-J., Gilfanov, M., & Sunyaev, R. 2003, MNRAS, 339, 793
Hawarden, T. G., van Woerden, H., Goss, W. M., Mebold, U., & Peterson, B. A. 1979, A&A, 76, 230
Høg, E., Fabricius, C., Makarov, V. V., et al. 2000, A&A, 355, L27
Huchra, J. P., Macri, L. M., Masters, K. L., et al. 2012, ApJS, 199, 26
Ishibashi, W. & Courvoisier, T. J.-L. 2010, A&A, 512, A58
Jarrett, T. H., Chester, T., Cutri, R., Schneider, S. E., & Huchra, J. P. 2003, AJ, 125, 525
Jenkins, L. P., Brandt, W. N., Colbert, E. J. M., et al. 2011, ApJ, 734, 33
Johnson, H. L. 1966, ARA&A, 4, 193
Kaastra, J. S. & Mewe, R. 2000, in Atomic Data Needs for X-ray Astronomy, ed. M. A. Bautista, T. R. Kallman, & A. K. Pradhan, 161
Kalberla, P. M. W., Burton, W. B., Hartmann, D., et al. 2005, A&A, 440, 775
Kalberla, P. M. W. & Kerp, J. 2009, ARA&A, 47, 27
Kinman, T. D. 1978, AJ, 83, 764
Koribalski, B. S. & López-Sánchez, Á. R. 2009, MNRAS, 400, 1749
Koribalski, B. S., Staveley-Smith, L., Kilborn, V. A., et al. 2004, AJ, 128, 16
Krautter, J., Zickgraf, F.-J., Appenzeller, I., et al. 1999, A&A, 350, 743
Kuntz, K. D. & Snowden, S. L. 2008, A&A, 478, 575
Kuntz, K. D. & Snowden, S. L. 2010, ApJS, 188, 46
Kuntz, K. D., Snowden, S. L., Pence, W. D., & Mukai, K. 2003, ApJ, 588, 264
Lin, D., Webb, N. A., & Barret, D. 2012, ApJ, 756, 27
Maccacaro, T., Gioia, I. M., Wolter, A., Zamorani, G., & Stocke, J. T. 1988, ApJ, 326, 680
Maddox, S. J., Efstathiou, G., Sutherland, W. J., & Loveday, J. 1990, MNRAS, 243, 692
Makishima, K., Maejima, Y., Mitsuda, K., et al. 1986, ApJ, 308, 635
Mauch, T., Murphy, T., Buttery, H. J., et al. 2003, MNRAS, 342, 1117
Mewe, R., Drake, S. A., Kaastra, J. S., et al. 1998, A&A, 339, 545
Mineo, S., Gilfanov, M., & Sunyaev, R. 2012a, MNRAS, 419, 2095
Mineo, S., Gilfanov, M., & Sunyaev, R. 2012b, MNRAS, 426, 1870
Monet, D. G. 1998, in Bulletin of the American Astronomical Society, Vol. 30, American Astronomical Society Meeting Abstracts, #120.03
Monet, D. G., Levine, S. E., Canzian, B., et al. 2003, AJ, 125, 984
Ochsenbein, F., Bauer, P., & Marcout, J. 2000, A&AS, 143, 23
O'Sullivan, E., Forbes, D. A., & Ponman, T. J. 2001, MNRAS, 328, 461
Page, M. J., Breeveld, A. A., Soria, R., et al. 2003, A&A, 400, 145
Park, T., Kashyap, V. L., Siemiginowska, A., et al. 2006, ApJ, 652, 610
Pickles, A. J. 1998, PASP, 110, 863
Pietsch, W., Misanovic, Z., Haberl, F., et al. 2004, A&A, 426, 11
Prestwich, A. H., Irwin, J. A., Kilgard, R. E., et al. 2003, ApJ, 595, 719
Primini, F. A., Forman, W., & Jones, C. 1993, ApJ, 410, 615
Revnivtsev, M., Churazov, E., Sazonov, S., Forman, W., & Jones, C. 2007, A&A, 473, 783
Revnivtsev, M., Churazov, E., Sazonov, S., Forman, W., & Jones, C. 2008, A&A, 490, 37
Robertson, I. P. & Cravens, T. E. 2003, Geophys. Res. Lett., 30, 1439
Roeser, S., Demleitner, M., & Schilbach, E. 2010, AJ, 139, 2440
Sazonov, S., Revnivtsev, M., Gilfanov, M., Churazov, E., & Sunyaev, R. 2006, A&A, 450, 117
Schlegel, E. M., Holt, S. S., & Petre, R. 2003, ApJ, 598, 982
Shirey, R., Soria, R., Borozdin, K., et al. 2001, A&A, 365, L195
Shlosman, I., Begelman, M. C., & Frank, J. 1990, Nature, 345, 679
Skrutskie, M. F., Cutri, R. M., Stiening, R., et al. 2006, AJ, 131, 1163
Smith, R. K., Brickhouse, N. S., Liedahl, D. A., & Raymond, J. C. 2001, ApJ, 556, L91
Snowden, S. L., Collier, M. R., & Kuntz, K. D. 2004, ApJ, 610, 1182
Snowden, S. L., Mushotzky, R. F., Kuntz, K. D., & Davis, D. S. 2008, A&A, 478, 615
Soria, R. & Wu, K. 2003, A&A, 410, 53
Stobbart, A.-M., Roberts, T. P., & Wilms, J. 2006, MNRAS, 368, 397
Strickland, D. K. & Heckman, T. M. 2009, ApJ, 697, 2030
Sutherland, R. S. & Dopita, M. A. 1993, ApJS, 88, 253
Tyler, K., Quillen, A. C., LaPage, A., & Rieke, G. H. 2004, ApJ, 610, 213
Ungruhe, R., Seitter, W. C., & Duerbeck, H. W. 2003, Journal of Astronomical Data, 9, 1
White, N. E., Nagase, F., & Parmar, A. N. 1995, X-ray Binaries, 1
Wilms, J., Allen, A., & McCray, R. 2000, ApJ, 542, 914
Zacharias, N., Finch, C. T., Girard, T. M., et al. 2013, AJ, 145, 44

Table A.1. Best-fitting parameters of the X-ray spectra of source No. 9 (errors at 90% confidence level). The flux (erg cm^{-2} s^{-1}) has been calculated in the energy range 0.2 – 2 keV.

	one-temperature model	two-temperature model
$N_{\rm H}$ (10^{22} cm^{-2})	$0.03^{+0.02}_{-0.02}$	$0.004^{+0.010}_{-0.004}$
kT_1 (keV)	$0.84^{+0.45}_{-0.47}$	$0.61^{+0.08}_{-0.22}$
norm.	$5.1^{+1.1}_{-0.9} \times 10^{-4}$	$1.2^{+0.4}_{-0.5} \times 10^{-4}$
kT_2 (keV)		$1.2^{+0.2}_{-0.2}$
norm.		$2.2^{+4.5}_{-4.4} \times 10^{-4}$
Abundances	$0.09^{+0.03}_{-0.02}$	0.2
χ^2_ν (d.o.f.)	1.25 (81)	1.04 (80)
$F_{\rm x}$	$2.5^{+1.2}_{-0.8} \times 10^{-13}$	$2.6^{+0.8}_{-1.0} \times 10^{-13}$
unabs. $F_{\rm x}$	$3.4^{+1.1}_{-0.8} \times 10^{-13}$	$2.9^{+0.8}_{-0.9} \times 10^{-13}$

Appendix A: classification and identification of the *XMM-Newton* sources

Appendix A.1: foreground stars

Source No. 9 Source No. 9 is the brightest X-ray source in the *XMM-Newton* observation of NGC 1512/1510. It is located outside of the optical discs of NGC 1512 and NGC 1510 (angular separation of $\sim 0.21^\circ$ from the nuclear region of NGC 1512). It is associated with the optical source USNO-B1 0464-0031154 and the infrared source 2MASS 04030715-4330273. It is close to the galaxy MRSS 250-130342 (Ungruhe et al. 2003) (angular separation of 15.3″), but the error circles do not overlap. Therefore, the galaxy is probably not associated with source No. 9.

Source No. 9 is bright enough in the *XMM-Newton* observation to allow a spectral analysis. We fitted the PN, MOS1, MOS2 spectra simultaneously with the thermal palsma model of Kaastra & Mewe (2000) (`mekal` in `XSPEC`), which is commonly used to study the X-ray coronal emission from stars. We first attempted to fit the spectrum with one-temperature model, but we obtained a poor fit with $\chi^2_\nu = 1.25$. Then, we fitted the spectrum with a two-temperature model, using non-solar abundances, which led to a significant improvement of the fit (Table A.1 and Fig. 8). We obtained the best-fit assuming metal abundances with regard to solar abundances of 0.2. Observations of under- or over-abundances of elements are not unusual in the coronae of stars (see e.g. Mewe et al. 1998; Favata 1998). We point out that in our fit the coronal abundances cannot be adequately constrained because of the poor statistics.

Sources No. 13 and 94 Sources No. 13 and 94 have optical, infrared, and radio counterparts. The radio counterparts, detected with ATCA, have fluxes of 0.9 mJy beam^{-1} (No. 13) and 0.3 mJy beam^{-1} (No. 94) at 20-cm (beam size: 7.599×5.470 arcsec^2). Although the measurement of a proper motion classify them as foreground stars[12] they violate the $\log_{10}(f_{\rm x}/f_{\rm opt}) \leq -1$ (No. 13) and $HR_3 \lesssim -0.4$ and $J - K_{\rm s}$ vs. $B - R$ of Fig. 7 (No. 94) criteria. The high $f_{\rm x}/f_{\rm opt}$ ratio of source No. 13 can be explained by the strong X-ray and radio emission of a low-mass pre-main sequence star (e.g. Getman et al. 2008; Carkner et al. 1997 and references therein). The hard HR_3 of No. 94 may indicate a binary nature (with an accreting neutron star in a propeller state).

Appendix A.2: background objects

Source No. 23 Source No. 23 is located outside of the D_{25} ellipse of NGC 1512 (6.3′ from the nuclear region of NGC 1512). It has neither an optical nor an infrared counterpart. A radio counterpart has been detected with ATCA with a flux of 0.3 mJy beam^{-1} at 20-cm (beam size: 8.000×8.000 arcsec^2). The *XMM-Newton* spectrum can be well fitted with an absorbed power-law (see Table 7 and Fig. 8). Therefore, we classified source No. 23 as an AGN candidate.

Appendix B: X-ray source catalogue of the *XMM-Newton* observation of the NGC 1512/1510 system

[12] We point out that the measurement of the proper motion of No. 94 in PPMXL catalogue ruled out the previous classification of this source as a galaxy (MRSS 250-123273 in the MRSS catalogue; APMUKS(BJ) B040305.24-433329.9 in the *The APM galaxy survey*, Maddox et al. 1990).

Table B.1. *(Only in the electronic version)* NGC 1512/1510 sources detected by *XMM-Newton*

No.	RA(2000)	DEC(2000)	pos. err.	rate (0.2 – 12 keV)	likelihood	HR1	HR2	HR3	HR4
1	04 02 42.04	−43 16 38.7	1.27″	0.0042 ± 0.0008	35.49	$0.35^{+0.41}_{-0.30}$	$0.31^{+0.25}_{-0.22}$	$-0.51^{+0.23}_{-0.30}$	$-0.39^{+0.15}_{-0.61}$
2	04 02 55.40	−43 22 02.3	1.81″	0.0047 ± 0.0013	8.44	$0.32^{+0.61}_{-0.25}$	$-0.15^{+0.44}_{-0.53}$	$0.211^{+0.54}_{-0.38}$	$-0.48^{+0.13}_{-0.52}$
3	04 02 59.32	−43 19 18.3	1.22″	0.0073 ± 0.0014	44.16	$0.30^{+0.24}_{-0.22}$	$-0.14^{+0.22}_{-0.23}$	$-0.45^{+0.26}_{-0.36}$	$-0.34^{+0.17}_{-0.66}$
4	04 02 59.40	−43 32 23.6	1.38″	0.0114 ± 0.0029	21.72	$0.59^{+0.36}_{-0.14}$	$-0.32^{+0.28}_{-0.31}$	$-0.40^{+0.15}_{-0.60}$	$0.01^{+0.56}_{-0.58}$
5	04 03 02.96	−43 15 47.3	2.03″	0.0037 ± 0.0012	8.07	$0.21^{+0.79}_{-0.26}$	$-0.21^{+0.26}_{-0.79}$	$0.51^{+0.49}_{-0.11}$	$-0.44^{+0.13}_{-0.56}$
6	04 03 03.12	−43 24 15.4	1.26″	0.0049 ± 0.0013	10.76	$0.32^{+0.48}_{-0.30}$	$-0.48^{+0.13}_{-0.53}$	$0.45^{+0.55}_{-0.13}$	$-0.40^{+0.20}_{-0.54}$
7	04 03 03.72	−43 28 18.5	1.00″	0.0092 ± 0.0016	31.61	$0.63^{+0.37}_{-0.08}$	$0.22^{+0.35}_{-0.27}$	$-0.46^{+0.22}_{-0.41}$	$-0.24^{+0.24}_{-0.72}$
8	04 03 05.55	−43 21 18.4	1.18″	0.0043 ± 0.0011	22.18	$0.41^{+0.43}_{-0.24}$	$0.19^{+0.32}_{-0.26}$	$-0.65^{+0.08}_{-0.35}$	$-0.16^{+0.27}_{-0.84}$
9	04 03 07.15	−43 30 29.0	0.18″	0.2757 ± 0.0063	5692.49	$0.40^{+0.03}_{-0.03}$	$-0.33^{+0.03}_{-0.03}$	$-0.78^{+0.05}_{-0.05}$	$-0.77^{+0.08}_{-0.22}$
10	04 03 08.30	−43 31 33.9	1.27″	0.0088 ± 0.0024	11.37	$0.51^{+0.49}_{-0.12}$	$-0.18^{+0.41}_{-0.49}$	$0.29^{+0.52}_{-0.31}$	$-0.49^{+0.12}_{-0.51}$
11	04 03 09.95	−43 15 56.3	0.93″	0.0103 ± 0.0014	76.62	$0.21^{+0.45}_{-0.36}$	$0.55^{+0.21}_{-0.18}$	$0.03^{+0.17}_{-0.15}$	$-0.73^{+0.11}_{-0.22}$
12	04 03 11.98	−43 20 32.6	1.77″	0.0040 ± 0.0010	11.61	$-0.02^{+0.58}_{-0.67}$	$0.16^{+0.84}_{-0.27}$	$0.58^{+0.39}_{-0.13}$	$-0.58^{+0.15}_{-0.38}$
13	04 03 12.96	−43 11 57.6	0.89″	0.0098 ± 0.0015	50.03	$0.70^{+0.30}_{-0.06}$	$0.22^{+0.25}_{-0.24}$	$-0.34^{+0.27}_{-0.27}$	$-0.46^{+0.14}_{-0.52}$
14	04 03 13.46	−43 28 02.0	1.35″	0.0070 ± 0.0016	13.91	$0.34^{+0.66}_{-0.18}$	$-0.36^{+0.17}_{-0.64}$	$0.60^{+0.40}_{-0.09}$	$-0.48^{+0.17}_{-0.48}$
15	04 03 17.87	−43 14 58.0	0.94″	0.0102 ± 0.0015	68.50	$0.54^{+0.27}_{-0.19}$	$0.11^{+0.21}_{-0.19}$	$-0.50^{+0.23}_{-0.27}$	$-0.25^{+0.32}_{-0.56}$
16	04 03 20.13	−43 25 36.9	1.50″	0.0063 ± 0.0012	19.95	$0.53^{+0.47}_{-0.09}$	$0.56^{+0.28}_{-0.20}$	$-0.35^{+0.26}_{-0.26}$	$-0.11^{+0.36}_{-0.40}$
17	04 03 20.51	−43 17 59.9	0.84″	0.0085 ± 0.0010	80.36	$0.06^{+0.18}_{-0.19}$	$-0.09^{+0.19}_{-0.19}$	$-0.06^{+0.21}_{-0.21}$	$-0.67^{+0.08}_{-0.33}$
18	04 03 21.47	−43 10 10.6	1.37″	0.0057 ± 0.0014	12.30	$0.46^{+0.54}_{-0.13}$	$0.06^{+0.33}_{-0.36}$	$-0.30^{+0.34}_{-0.42}$	$-0.18^{+0.36}_{-0.63}$
19	04 03 21.87	−43 24 55.2	0.66″	0.0199 ± 0.0017	149.95	$-0.09^{+0.12}_{-0.13}$	$-0.29^{+0.14}_{-0.16}$	$-0.51^{+0.21}_{-0.26}$	$0.14^{+0.37}_{-0.36}$
20	04 03 22.09	−43 12 28.4	1.32″	0.0036 ± 0.0010	8.43	$0.42^{+0.54}_{-0.18}$	$-0.02^{+0.37}_{-0.36}$	$-0.55^{+0.11}_{-0.45}$	$0.28^{+0.72}_{-0.20}$
21	04 03 22.27	−43 25 12.3	0.56″	0.0349 ± 0.0028	294.29	$0.01^{+0.16}_{-0.16}$	$-0.26^{+0.19}_{-0.19}$	$0.13^{+0.22}_{-0.21}$	$-0.81^{+0.04}_{-0.19}$
22	04 03 23.19	−43 17 17.3	0.88″	0.0087 ± 0.0011	63.40	$0.47^{+0.39}_{-0.23}$	$0.10^{+0.28}_{-0.24}$	$-0.29^{+0.27}_{-0.31}$	$-0.09^{+0.36}_{-0.40}$
23	04 03 25.37	−43 17 22.0	0.30″	0.0541 ± 0.0020	1709.88	$0.53^{+0.05}_{-0.05}$	$-0.17^{+0.05}_{-0.05}$	$-0.64^{+0.06}_{-0.06}$	$-0.46^{+0.18}_{-0.17}$
24	04 03 25.76	−43 23 10.0	0.74″	0.0112 ± 0.0011	136.76	$0.00^{+0.17}_{-0.17}$	$-0.15^{+0.19}_{-0.19}$	$-0.37^{+0.29}_{-0.28}$	$-0.17^{+0.39}_{-0.50}$
25	04 03 26.52	−43 21 46.3	0.89″	0.0049 ± 0.0008	29.71	$0.15^{+0.66}_{-0.38}$	$0.44^{+0.39}_{-0.25}$	$-0.06^{+0.31}_{-0.29}$	$-0.26^{+0.34}_{-0.41}$
26	04 03 28.37	−43 29 29.5	0.61″	0.0220 ± 0.0019	203.27	$0.22^{+0.13}_{-0.13}$	$-0.27^{+0.13}_{-0.13}$	$-0.39^{+0.23}_{-0.21}$	$-0.27^{+0.30}_{-0.38}$
27	04 03 30.29	−43 31 09.6	1.13″	0.0092 ± 0.0018	26.23	$0.42^{+0.58}_{-0.15}$	$0.04^{+0.42}_{-0.41}$	$0.07^{+0.43}_{-0.36}$	$-0.49^{+0.12}_{-0.51}$
28	04 03 32.12	−43 21 39.2	0.38″	0.0119 ± 0.0010	205.28	$0.80^{+0.20}_{-0.05}$	$-0.10^{+0.16}_{-0.16}$	$-0.28^{+0.22}_{-0.21}$	$-0.67^{+0.08}_{-0.33}$
29	04 03 32.71	−43 24 01.7	1.30″	0.0169 ± 0.0015	143.73	$0.39^{+0.15}_{-0.14}$	$-0.60^{+0.14}_{-0.16}$	$-0.10^{+0.38}_{-0.33}$	$-0.23^{+0.36}_{-0.52}$
30	04 03 35.40	−43 17 45.8	0.48″	0.0207 ± 0.0013	369.67	$0.12^{+0.14}_{-0.13}$	$-0.26^{+0.13}_{-0.15}$	$-0.47^{+0.21}_{-0.23}$	$0.03^{+0.38}_{-0.36}$
31	04 03 36.55	−43 16 09.1	1.24″	0.0047 ± 0.0009	17.29	$0.25^{+0.50}_{-0.35}$	$-0.28^{+0.33}_{-0.51}$	$0.45^{+0.43}_{-0.22}$	$-0.24^{+0.33}_{-0.37}$
32	04 03 36.61	−43 11 57.0	1.13″	0.0070 ± 0.0012	28.61	$0.13^{+0.38}_{-0.34}$	$0.02^{+0.35}_{-0.34}$	$-0.28^{+0.34}_{-0.45}$	$-0.43^{+0.14}_{-0.58}$
33	04 03 37.26	−43 17 31.9	0.47″	0.0129 ± 0.0011	209.76	$0.78^{+0.22}_{-0.05}$	$0.13^{+0.20}_{-0.18}$	$0.09^{+0.17}_{-0.17}$	$-0.72^{+0.09}_{-0.27}$
34	04 03 37.46	−43 11 05.9	1.57″	0.0043 ± 0.0012	7.62	$-0.05^{+0.33}_{-0.31}$	$-0.22^{+0.32}_{-0.40}$	$-0.47^{+0.13}_{-0.53}$	$0.33^{+0.67}_{-0.18}$
35	04 03 37.63	−43 27 38.8	0.94″	0.0095 ± 0.0013	60.41	$0.14^{+0.26}_{-0.26}$	$0.10^{+0.23}_{-0.22}$	$-0.32^{+0.26}_{-0.27}$	$-0.29^{+0.33}_{-0.46}$
36	04 03 37.69	−43 09 09.0	1.10″	0.0120 ± 0.0017	57.48	$-0.11^{+0.25}_{-0.25}$	$0.31^{+0.21}_{-0.21}$	$-0.42^{+0.23}_{-0.23}$	$-0.48^{+0.15}_{-0.49}$
37	04 03 38.08	−43 24 21.6	1.20″	0.0026 ± 0.0006	8.29	$0.22^{+0.78}_{-0.23}$	$0.23^{+0.53}_{-0.34}$	$-0.13^{+0.40}_{-0.49}$	$-0.22^{+0.30}_{-0.69}$
38	04 03 38.24	−43 10 05.4	0.66″	0.0199 ± 0.0018	168.78	$-0.04^{+0.16}_{-0.16}$	$0.00^{+0.17}_{-0.18}$	$-0.14^{+0.20}_{-0.19}$	$-0.72^{+0.07}_{-0.28}$
39	04 03 39.09	−43 31 02.0	1.77″	0.0073 ± 0.0016	15.43	$0.34^{+0.58}_{-0.25}$	$0.04^{+0.41}_{-0.37}$	$-0.05^{+0.37}_{-0.42}$	$-0.39^{+0.19}_{-0.58}$
40	04 03 40.85	−43 28 57.1	1.68″	0.0082 ± 0.0017	18.70	$0.29^{+0.64}_{-0.24}$	$0.22^{+0.44}_{-0.34}$	$-0.55^{+0.11}_{-0.45}$	$0.01^{+0.68}_{-0.61}$
41	04 03 41.82	−43 10 18.3	0.71″	0.0215 ± 0.0019	200.03	$0.29^{+0.22}_{-0.22}$	$0.22^{+0.16}_{-0.15}$	$-0.25^{+0.16}_{-0.16}$	$-0.52^{+0.20}_{-0.24}$
42	04 03 42.10	−43 18 38.5	1.18″	0.0029 ± 0.0006	11.49	$0.33^{+0.67}_{-0.19}$	$0.45^{+0.49}_{-0.19}$	$-0.40^{+0.24}_{-0.50}$	$0.06^{+0.61}_{-0.48}$
43	04 03 42.40	−43 19 58.9	0.55″	0.0105 ± 0.0009	166.39	$0.26^{+0.15}_{-0.14}$	$-0.32^{+0.15}_{-0.15}$	$-0.69^{+0.08}_{-0.31}$	$0.12^{+0.72}_{-0.39}$
44	04 03 42.72	−43 23 17.1	1.46″	0.0025 ± 0.0006	10.36	$-0.04^{+0.53}_{-0.62}$	$0.08^{+0.68}_{-0.46}$	$0.44^{+0.49}_{-0.20}$	$-0.56^{+0.11}_{-0.44}$
45	04 03 42.90	−43 20 50.2	1.41″	0.0027 ± 0.0006	8.80	$0.44^{+0.57}_{-0.14}$	$0.01^{+0.36}_{-0.39}$	$0.06^{+0.40}_{-0.33}$	$-0.39^{+0.18}_{-0.59}$
46	04 03 42.94	−43 16 01.3	0.38″	0.0148 ± 0.0011	272.46	$0.13^{+0.14}_{-0.14}$	$-0.08^{+0.13}_{-0.13}$	$-0.27^{+0.16}_{-0.16}$	$-0.55^{+0.21}_{-0.31}$
47	04 03 45.43	−43 26 31.9	1.14″	0.0062 ± 0.0013	20.24	$0.48^{+0.52}_{-0.13}$	$0.18^{+0.47}_{-0.36}$	$-0.26^{+0.34}_{-0.51}$	$-0.25^{+0.21}_{-0.75}$
48	04 03 47.11	−43 24 42.8	1.52″	0.0032 ± 0.0008	6.59	$-0.19^{+0.27}_{-0.81}$	$0.28^{+0.72}_{-0.22}$	$0.24^{+0.69}_{-0.27}$	$0.02^{+0.49}_{-0.47}$
49	04 03 48.29	−43 10 11.7	1.20″	0.0092 ± 0.0014	37.38	$0.47^{+0.53}_{-0.13}$	$0.38^{+0.26}_{-0.25}$	$-0.52^{+0.24}_{-0.31}$	$-0.33^{+0.17}_{-0.67}$
50	04 03 48.97	−43 14 54.4	0.78″	0.0068 ± 0.0009	48.67	$-0.15^{+0.37}_{-0.44}$	$0.31^{+0.42}_{-0.28}$	$0.19^{+0.30}_{-0.29}$	$-0.52^{+0.18}_{-0.41}$
51	04 03 50.86	−43 22 04.9	1.54″	0.0027 ± 0.0006	13.36	$-0.09^{+0.45}_{-0.70}$	$0.55^{+0.45}_{-0.11}$	$-0.38^{+0.29}_{-0.41}$	$-0.18^{+0.32}_{-0.73}$
52	04 03 50.91	−43 24 40.1	1.07″	0.0031 ± 0.0007	14.07	$0.13^{+0.87}_{-0.29}$	$0.38^{+0.62}_{-0.16}$	$0.29^{+0.37}_{-0.31}$	$-0.52^{+0.13}_{-0.48}$
53	04 03 52.76	−43 20 59.0	1.31″	0.0030 ± 0.0009	7.72	$0.14^{+0.42}_{-0.37}$	$-0.27^{+0.32}_{-0.47}$	$-0.03^{+0.50}_{-0.52}$	$-0.22^{+0.23}_{-0.78}$
54	04 03 54.26	−43 20 56.7	0.21″	0.0697 ± 0.0020	2705.45	$0.22^{+0.06}_{-0.05}$	$-0.31^{+0.05}_{-0.05}$	$-0.37^{+0.07}_{-0.08}$	$-0.46^{+0.14}_{-0.13}$
55	04 03 54.30	−43 18 53.0	0.94″	0.0044 ± 0.0007	29.10	$0.33^{+0.50}_{-0.30}$	$0.24^{+0.31}_{-0.28}$	$-0.14^{+0.28}_{-0.29}$	$-0.22^{+0.37}_{-0.39}$

Continued on next page

Continued from previous page

No.	RA(2000)	DEC(2000)	pos. err.	rate (0.2 – 12 keV)	likelihood	HR1	HR2	HR3	HR4
56	04 03 54.52	−43 14 32.6	1.76″	0.0031 ± 0.0007	10.63	$-0.43^{+0.14}_{-0.57}$	$0.19^{+0.81}_{-0.25}$	$0.53^{+0.47}_{-0.12}$	$-0.30^{+0.33}_{-0.40}$
57	04 03 54.79	−43 22 24.5	1.42″	0.0048 ± 0.0019	6.25	$0.34^{+0.66}_{-0.19}$	$0.26^{+0.57}_{-0.32}$	$-0.34^{+0.18}_{-0.66}$	$0.15^{+0.80}_{-0.30}$
58	04 03 55.58	−43 09 45.8	0.44″	0.0458 ± 0.0025	706.75	$0.07^{+0.08}_{-0.08}$	$-0.30^{+0.09}_{-0.09}$	$-0.51^{+0.15}_{-0.16}$	$-0.18^{+0.26}_{-0.29}$
59	04 03 56.14	−43 17 20.7	0.52″	0.0143 ± 0.0010	286.01	$0.26^{+0.12}_{-0.12}$	$-0.29^{+0.11}_{-0.12}$	$-0.32^{+0.18}_{-0.18}$	$-0.46^{+0.27}_{-0.37}$
60	04 03 56.36	−43 08 30.7	1.08″	0.0168 ± 0.0037	37.73	$0.56^{+0.44}_{-0.11}$	$0.25^{+0.32}_{-0.26}$	$0.19^{+0.24}_{-0.23}$	$-0.52^{+0.20}_{-0.24}$
61	04 03 56.60	−43 29 05.0	1.61″	0.0056 ± 0.0011	16.82	$0.25^{+0.33}_{-0.31}$	$-0.65^{+0.08}_{-0.35}$	$0.14^{+0.82}_{-0.31}$	$-0.30^{+0.19}_{-0.70}$
62	04 03 58.34	−43 22 46.0	1.20″	0.0047 ± 0.0008	26.37	$0.19^{+0.52}_{-0.38}$	$0.20^{+0.35}_{-0.35}$	$0.47^{+0.19}_{-0.17}$	$-0.61^{+0.19}_{-0.24}$
63	04 04 00.99	−43 23 19.0	0.23″	0.0687 ± 0.0023	2309.37	$-0.01^{+0.06}_{-0.05}$	$-0.23^{+0.06}_{-0.06}$	$-0.52^{+0.08}_{-0.09}$	$-0.49^{+0.20}_{-0.19}$
64	04 04 01.23	−43 33 23.2	1.98″	0.0211 ± 0.0092	12.21	$-0.13^{+0.37}_{-0.49}$	$0.21^{+0.47}_{-0.33}$	$-0.41^{+0.15}_{-0.59}$	$-0.39^{+0.15}_{-0.61}$
65	04 04 03.38	−43 25 38.4	1.20″	0.0043 ± 0.0009	19.54	$0.26^{+0.74}_{-0.21}$	$0.36^{+0.48}_{-0.28}$	$0.06^{+0.35}_{-0.33}$	$-0.37^{+0.28}_{-0.45}$
66	04 04 08.28	−43 14 14.9	1.04″	0.0075 ± 0.0025	27.53	$-0.14^{+0.40}_{-0.53}$	$0.63^{+0.29}_{-0.15}$	$-0.59^{+0.17}_{-0.34}$	$-0.34^{+0.18}_{-0.66}$
67	04 04 08.90	−43 18 43.8	1.31″	0.0027 ± 0.0006	7.70	$0.28^{+0.37}_{-0.30}$	$-0.47^{+0.22}_{-0.42}$	$0.19^{+0.55}_{-0.38}$	$-0.43^{+0.15}_{-0.57}$
68	04 04 10.89	−43 07 03.6	2.10″	0.0170 ± 0.0025	50.21	$0.30^{+0.70}_{-0.20}$	$0.55^{+0.35}_{-0.18}$	$0.01^{+0.25}_{-0.26}$	$-0.56^{+0.19}_{-0.31}$
69	04 04 11.17	−43 19 57.7	0.72″	0.0083 ± 0.0009	95.23	$0.31^{+0.26}_{-0.25}$	$0.24^{+0.18}_{-0.18}$	$-0.40^{+0.20}_{-0.19}$	$-0.50^{+0.13}_{-0.50}$
70	04 04 11.19	−43 16 58.8	0.82″	0.0068 ± 0.0009	66.41	$0.47^{+0.28}_{-0.23}$	$-0.05^{+0.21}_{-0.22}$	$-0.28^{+0.28}_{-0.27}$	$-0.32^{+0.31}_{-0.48}$
71	04 04 12.64	−43 22 30.7	0.81″	0.0068 ± 0.0008	79.81	$0.70^{+0.30}_{-0.07}$	$0.03^{+0.22}_{-0.21}$	$-0.12^{+0.22}_{-0.24}$	$-0.42^{+0.30}_{-0.40}$
72	04 04 13.90	−43 29 00.1	1.13″	0.0121 ± 0.0017	67.72	$0.79^{+0.21}_{-0.04}$	$0.01^{+0.24}_{-0.23}$	$-0.03^{+0.24}_{-0.25}$	$-0.76^{+0.05}_{-0.24}$
73	04 04 14.97	−43 22 57.6	0.79″	0.0083 ± 0.0010	77.13	$-0.05^{+0.21}_{-0.21}$	$-0.29^{+0.24}_{-0.26}$	$-0.01^{+0.35}_{-0.33}$	$-0.40^{+0.23}_{-0.51}$
74	04 04 15.17	−43 22 34.3	1.61″	0.0025 ± 0.0007	9.05	$0.60^{+0.40}_{-0.10}$	$0.17^{+0.31}_{-0.28}$	$-0.51^{+0.19}_{-0.39}$	$0.14^{+0.60}_{-0.39}$
75	04 04 15.21	−43 24 09.8	1.40″	0.0028 ± 0.0008	8.97	$0.33^{+0.38}_{-0.28}$	$-0.19^{+0.33}_{-0.35}$	$-0.42^{+0.15}_{-0.58}$	$0.08^{+0.77}_{-0.42}$
76	04 04 15.72	−43 31 49.2	1.23″	0.0109 ± 0.0021	33.95	$0.27^{+0.33}_{-0.32}$	$-0.41^{+0.28}_{-0.37}$	$-0.22^{+0.27}_{-0.73}$	$-0.22^{+0.23}_{-0.78}$
77	04 04 15.79	−43 28 03.7	0.87″	0.0120 ± 0.0015	77.02	$0.30^{+0.30}_{-0.25}$	$0.13^{+0.24}_{-0.22}$	$-0.46^{+0.21}_{-0.28}$	$-0.28^{+0.33}_{-0.55}$
78	04 04 17.53	−43 19 06.8	1.18″	0.0033 ± 0.0007	10.36	$0.29^{+0.65}_{-0.24}$	$-0.15^{+0.39}_{-0.55}$	$-0.19^{+0.30}_{-0.73}$	$0.06^{+0.69}_{-0.49}$
79	04 04 17.77	−43 25 47.5	0.95″	0.0108 ± 0.0014	65.43	$0.66^{+0.34}_{-0.09}$	$0.34^{+0.19}_{-0.18}$	$-0.39^{+0.18}_{-0.19}$	$-0.36^{+0.30}_{-0.36}$
80	04 04 17.94	−43 29 13.2	1.18″	0.0070 ± 0.0016	19.29	$0.00^{+0.57}_{-0.50}$	$0.44^{+0.46}_{-0.22}$	$0.10^{+0.29}_{-0.29}$	$-0.65^{+0.08}_{-0.35}$
81	04 04 20.21	−43 24 30.3	1.04″	0.0048 ± 0.0009	19.93	$0.17^{+0.71}_{-0.34}$	$0.45^{+0.42}_{-0.22}$	$0.07^{+0.30}_{-0.29}$	$-0.64^{+0.09}_{-0.36}$
82	04 04 21.24	−43 22 23.4	1.62″	0.0029 ± 0.0008	7.20	$0.30^{+0.66}_{-0.22}$	$-0.36^{+0.17}_{-0.64}$	$0.36^{+0.65}_{-0.17}$	$-0.32^{+0.18}_{-0.68}$
83	04 04 22.57	−43 24 52.3	1.70″	0.0036 ± 0.0009	10.77	$-0.03^{+0.57}_{-0.66}$	$0.50^{+0.50}_{-0.12}$	$0.12^{+0.36}_{-0.32}$	$-0.63^{+0.09}_{-0.37}$
84	04 04 23.05	−43 12 02.0	1.18″	0.0063 ± 0.0012	22.66	$0.12^{+0.36}_{-0.34}$	$-0.17^{+0.35}_{-0.38}$	$0.09^{+0.39}_{-0.38}$	$-0.48^{+0.13}_{-0.52}$
85	04 04 24.15	−43 25 46.3	1.42″	0.0045 ± 0.0012	8.05	$0.47^{+0.44}_{-0.20}$	$-0.24^{+0.35}_{-0.38}$	$-0.17^{+0.38}_{-0.56}$	$-0.28^{+0.20}_{-0.73}$
86	04 04 24.20	−43 13 43.2	1.21″	0.0072 ± 0.0014	19.86	$-0.05^{+0.34}_{-0.36}$	$-0.11^{+0.37}_{-0.40}$	$-0.24^{+0.34}_{-0.58}$	$0.32^{+0.54}_{-0.29}$
87	04 04 26.82	−43 28 40.7	1.03″	0.0077 ± 0.0015	25.75	$0.29^{+0.29}_{-0.25}$	$-0.34^{+0.28}_{-0.31}$	$-0.45^{+0.14}_{-0.56}$	$-0.13^{+0.28}_{-0.87}$
88	04 04 29.73	−43 23 13.9	1.43″	0.0030 ± 0.0009	7.51	$0.22^{+0.49}_{-0.37}$	$-0.11^{+0.42}_{-0.43}$	$-0.20^{+0.35}_{-0.64}$	$-0.16^{+0.26}_{-0.84}$
89	04 04 31.49	−43 26 10.4	1.42″	0.0072 ± 0.0018	18.81	$0.11^{+0.37}_{-0.34}$	$-0.58^{+0.10}_{-0.42}$	$0.03^{+0.77}_{-0.50}$	$0.09^{+0.77}_{-0.43}$
90	04 04 35.29	−43 20 06.7	1.33″	0.0054 ± 0.0011	22.06	$0.39^{+0.56}_{-0.19}$	$0.44^{+0.26}_{-0.24}$	$-0.57^{+0.20}_{-0.30}$	$-0.32^{+0.18}_{-0.68}$
91	04 04 37.22	−43 13 22.1	0.99″	0.0079 ± 0.0013	30.85	$0.31^{+0.34}_{-0.30}$	$-0.20^{+0.29}_{-0.31}$	$-0.30^{+0.33}_{-0.47}$	$-0.42^{+0.14}_{-0.58}$
92	04 04 38.05	−43 14 03.7	0.44″	0.0388 ± 0.0023	510.49	$0.21^{+0.10}_{-0.09}$	$-0.17^{+0.09}_{-0.10}$	$-0.54^{+0.15}_{-0.14}$	$-0.41^{+0.26}_{-0.34}$
93	04 04 41.89	−43 09 43.4	0.78″	0.0122 ± 0.0014	162.33	$0.18^{+0.22}_{-0.20}$	$0.19^{+0.18}_{-0.16}$	$-0.40^{+0.17}_{-0.20}$	$-0.67^{+0.08}_{-0.33}$
94	04 04 43.73	−43 25 22.9	1.43″	0.0057 ± 0.0015	12.83	$-0.55^{+0.11}_{-0.45}$	$0.18^{+0.83}_{-0.28}$	$0.17^{+0.79}_{-0.28}$	$-0.17^{+0.35}_{-0.70}$
95	04 04 46.15	−43 15 37.8	1.77″	0.0052 ± 0.0012	11.55	$0.47^{+0.54}_{-0.13}$	$0.20^{+0.40}_{-0.34}$	$-0.26^{+0.34}_{-0.42}$	$-0.19^{+0.36}_{-0.57}$
96	04 04 46.86	−43 29 11.3	1.06″	0.0089 ± 0.0020	16.51	$0.47^{+0.53}_{-0.13}$	$-0.14^{+0.40}_{-0.46}$	$0.05^{+0.49}_{-0.44}$	$-0.50^{+0.11}_{-0.50}$
97	04 04 47.02	−43 16 30.6	1.32″	0.0084 ± 0.0013	30.08	$-0.16^{+0.27}_{-0.27}$	$0.09^{+0.28}_{-0.30}$	$-0.33^{+0.33}_{-0.35}$	$-0.44^{+0.13}_{-0.56}$
98	04 04 47.14	−43 22 03.5	0.88″	0.0126 ± 0.0017	61.83	$-0.56^{+0.10}_{-0.44}$	$0.40^{+0.60}_{-0.15}$	$0.46^{+0.37}_{-0.23}$	$-0.25^{+0.27}_{-0.31}$
99	04 04 49.77	−43 20 43.8	0.88″	0.0150 ± 0.0018	84.92	$-0.01^{+0.29}_{-0.26}$	$0.37^{+0.20}_{-0.20}$	$-0.23^{+0.21}_{-0.19}$	$-0.49^{+0.23}_{-0.31}$
100	04 04 51.53	−43 19 03.8	1.32″	0.0088 ± 0.0016	24.31	$-0.08^{+0.29}_{-0.29}$	$-0.05^{+0.32}_{-0.33}$	$0.07^{+0.32}_{-0.31}$	$-0.45^{+0.24}_{-0.40}$
101	04 04 59.35	−43 13 32.7	0.69″	0.0091 ± 0.0010	150.06	$0.40^{+0.13}_{-0.13}$	$-0.25^{+0.13}_{-0.13}$	$-0.22^{+0.18}_{-0.18}$	$-0.56^{+0.20}_{-0.27}$
102	04 05 00.38	−43 14 46.5	1.06″	0.0108 ± 0.0021	34.43	$-0.11^{+0.46}_{-0.52}$	$0.40^{+0.44}_{-0.26}$	$0.05^{+0.30}_{-0.30}$	$-0.64^{+0.08}_{-0.36}$
103	04 05 02.17	−43 20 36.9	2.00″	0.0082 ± 0.0019	7.55	$0.17^{+0.59}_{-0.38}$	$0.06^{+0.48}_{-0.43}$	$-0.16^{+0.42}_{-0.55}$	$-0.03^{+0.44}_{-0.56}$
104	04 05 07.07	−43 18 31.6	1.26″	0.0088 ± 0.0019	24.88	$0.29^{+0.29}_{-0.26}$	$-0.61^{+0.11}_{-0.38}$	$0.11^{+0.65}_{-0.43}$	$-0.38^{+0.15}_{-0.63}$
105	04 05 09.57	−43 18 50.7	0.95″	0.0258 ± 0.0028	150.49	$0.31^{+0.14}_{-0.14}$	$-0.25^{+0.14}_{-0.13}$	$-0.60^{+0.20}_{-0.24}$	$-0.23^{+0.32}_{-0.56}$
106	04 05 11.59	−43 22 34.0	2.19″	0.0086 ± 0.0021	15.21	$-0.32^{+0.28}_{-0.32}$	$0.18^{+0.38}_{-0.33}$	$-0.60^{+0.10}_{-0.40}$	$-0.25^{+0.24}_{-0.76}$

Table B.2. *(Only in the electronic version)* NGC 1512/1510 sources detected by *XMM-Newton* cross-correlated with optical, infrared, and radio counterparts. For each source the identification proposed by the respective authors and our classification are given. Uncertain classifications are given in brackets.

No.	USNO B1	2MASS	optical	radio	class.
1	0467-0032009				
2					
3					
4	0464-0031137	04025923-4332221			foreground star
5					
6					
7					
8					
9	0464-0031154	04030715-4330273			foreground star
10	0464-0031159				
11					
12					
13	0468-0031995	04031316-4311583		ATCA 04 03 12.92 -43 11 56.0	foreground star
14					
15					
16					
17					
18					
19	0465-0031058				
20	0467-0032091				
21					
22					
23				ATCA 04 03 25.54 -43 17 23.2	background object
24					
25					
26	0465-0031069				
27					
28					
29			NGC1510	ATCA 04 03 32.69 -43 23 59.2	NGC 1510
30					
31					
32					
33					
34					
35					
36	0468-0032035				
37	0465-0031095				
38	0468-0032036				
39					
40	0465-0031108	04034120-4329015	TYC7583-1149-1		foreground star
41	0468-003204				
42					
43	0466-0031581				
44					
45					
46					
47					
48					
49					
50					
51					
52					
53					
54	0466-0031598	04035419-4320552	NGC1512	ATCA 04 03 54.20 -43 20 56.2	
55					
56	0467-0032138				
57					
58	0468-0032062				
59					
60					
61	0465-0031140	04035632-4329041	MRSS 250-126782		galaxy
62	0466-0031604				
63	0466-0031610	04040093-4323175			QSO or XRB
64					
65					
66					
67	0466-0031624			ATCA 04 04 08.82 -43 18 42.3	background object
68					
69					
70					
71				SUMSS J040412-432235 and ATCA source	background object
72					
73					
74					
75					
76					

Continued on next page

Continued from previous page

No.	USNO B1	2MASS	optical	radio	class.
77					
78					
79					
80					
81	0465-0031199				
82	0466-0031640	04042126-4322204			
83				ATCA 04 04 22.25 -43 24 52.1	background object
84					
85					
86					
87					
88					
89	0465-0031223	04043150-4326090	TYC583-426-1		foreground star
90					
91					
92	0467-0032209				
93	0468-0032147				
94	0465-0031250	04044352-4325227	MRSS 250-123273	ATCA 04 04 43.66 -43 25 22.5	foreground star
95					
96					
97					
98				ATCA 04 04 46.77 -43 22 02.2	background object
99	0466-0031693				
100					
101	0467-0032246				
102					
103					
104	0466-0031732				
105	0466-0031738				
106	0466-0031740				